

---

1 **An improved regional coupled modeling system for Arctic sea ice simulation and**  
2 **prediction: a case study for 2018**

3

4 **Chao-Yuan Yang<sup>1</sup>, Jiping Liu<sup>2</sup>, Dake Chen<sup>1</sup>**

5

6 <sup>1</sup>School of Atmospheric Sciences, Sun Yat-sen University, and Southern Marine Science and  
7 Engineering Guangdong Laboratory (Zhuhai), Zhuhai, Guangdong, China

8 <sup>2</sup>Department of Atmospheric and Environmental Sciences, University at Albany, State  
9 University of New York, Albany, NY, USA

10

11 Corresponding authors:

12 Chao-Yuan Yang ([yangchy36@mail.sysu.edu.cn](mailto:yangchy36@mail.sysu.edu.cn)) and Jiping Liu ([jliu26@albany.edu](mailto:jliu26@albany.edu))

13

14

---

15 **Abstract**

16       The improved/updated Coupled Arctic Prediction System (CAPS) is evaluated using a set  
17 of Pan-Arctic prediction experiments for the year 2018. CAPS is built on Weather Research  
18 and Forecasting model (WRF), the Regional Ocean Modeling System (ROMS), the  
19 Community Ice Code (CICE), and a data assimilation based on the Local Error Subspace  
20 Transform Kalman Filter. We analyze physical processes linking improved/changed physical  
21 parameterizations in WRF, ROMS, and CICE to changes in the simulated Arctic sea ice state.  
22 Our results show that the improved convection and boundary layer schemes in WRF result in  
23 an improved simulation of downward radiative fluxes and near surface air temperature, which  
24 influences the predicted ice thickness. The changed tracer advection and vertical mixing  
25 schemes in ROMS reduce the bias in sea surface temperature and change ocean temperature  
26 and salinity structure in the surface layer, leading to improved evolution of the predicted ice  
27 extent (particularly correcting the late ice recovery issue in the previous CAPS). The improved  
28 sea ice thermodynamics in CICE have noticeable influences on the predicted ice thickness. The  
29 updated CAPS can better predict the evolution of Arctic sea ice during the melting season  
30 compared with its predecessor, though the prediction still has some biases at the regional scale.  
31 We further show that the updated CAPS can remain skillful beyond the melting season, which  
32 may have potential values for stakeholders to make decisions for socioeconomical activities in  
33 the Arctic.

34

35

---

## 36 1. Introduction

37 Over the past few decades, the extent of Arctic sea ice has decreased rapidly and entered  
38 a thinner/younger regime associated with global climate change (e.g., Kwok, 2018; Serreze  
39 and Meier, 2019). The dramatic changes in the properties of Arctic sea ice have gained  
40 increasing attentions by a wide range of stakeholders, such as trans-Arctic shipping, natural  
41 resource exploration, and activities of coastal communities relying on sea ice (e.g., Newton et  
42 al., 2016). This leads to increasing demands on skillful Arctic sea ice prediction, particularly at  
43 seasonal timescale (e.g., Jung et al., 2016; Liu et al., 2019; Stroeve et al., 2014). However,  
44 Arctic sea ice predictions based on different approaches (e.g., statistical method and dynamical  
45 model) submitted to the Sea Ice Outlook, a community effort managed by the Sea Ice Prediction  
46 Network (SIPN, <https://www.arcus.org/sipn>), show substantial biases in the predicted seasonal  
47 minimum of Arctic sea ice extent compared to the observations for most years since 2008 (Liu  
48 et al., 2019; Stroeve et al., 2014).

49 Recently, we have developed an atmosphere-ocean-sea ice regional coupled modeling  
50 system for seasonal Arctic sea ice prediction (Yang et al., 2020, hereafter Y20), in which the  
51 Community Ice Code (CICE) is coupled with the Weather Research and Forecasting Model  
52 (WRF) and the Regional Ocean Modeling System (ROMS), hereafter called Coupled Arctic  
53 Prediction System (CAPS). To improve the accuracy of initial sea ice conditions, CAPS  
54 employs an ensemble-based data assimilation system to assimilate satellite-based sea ice  
55 observations. Seasonal Pan-Arctic sea ice predictions with improved initial sea ice conditions  
56 conducted in Y20 have shown that CAPS has the potential to provide skillful Arctic sea ice

---

57 prediction at seasonal timescale.

58 We know that the changes of sea ice variables (e.g., ice extent, ice concentration, ice  
59 thickness, ice drift) are mainly driven by forcings from the atmosphere and the ocean.  
60 Atmospheric cloudiness and related radiation influence surface ice melting (Huang et al., 2019;  
61 Kapsch et al., 2016; Kay et al., 2008) and the energy stored in the surface mixed layer that  
62 determines the seasonal ice melt and growth (e.g., Perovich et al., 2011, 2014). Atmospheric  
63 circulation is the primary driver for the transportation of sea ice and partly responsible for the  
64 variability of Arctic sea ice (e.g., Mallett et al., 2021; Ogi et al., 2010; Zhang et al., 2008).  
65 Olonscheck et al. (2019) suggested that atmospheric temperature fluctuations explain a  
66 majority of Arctic sea ice variability while other drivers (e.g., surface winds, and poleward heat  
67 transport) account for about 25% of Arctic sea ice variability. The oceanic heat inputs (as well  
68 as salt inputs) into the Arctic Ocean include the Atlantic Water (AW; Aagaard, 1989;  
69 McLaughlin et al., 2009) through the Barents Sea, and the Pacific Water (PW; Itoh et al., 2013;  
70 Woodgate et al., 2005) from the Bering Strait. The oceanic heat inputs from AW and PW are  
71 not directly available for sea ice since they are separated from a cold and fresh layer underlying  
72 sea ice (e.g., Carmack et al., 2015, Fig. 2). Vertical mixing by the internal wave (e.g., Fer, 2014)  
73 and double diffusion (e.g., Padman and Dillon, 1987; Turner, 1973) are the principal processes  
74 for upward heat transport from the subsurface layer (i.e., AW and PW) to the surface mixed  
75 layer in the Arctic Ocean. Sea ice thermodynamics determines how thermal properties of sea  
76 ice (e.g., temperature, salinity) change. These changes then influence the thermal structure of  
77 underlying ocean through interfacial fluxes (i.e., heat, salt and freshwater fluxes; DuVivier et

---

78 al., 2021; Kirkman IV and Bitz, 2011) and ice thickness (e.g., Bailey et al., 2020).

79 CAPS is configured for the Arctic with sufficient flexibility. That means each model  
80 component of CAPS (WRF, ROMS, and CICE) has different physics options for us to choose  
81 and capability to integrate ongoing improvements in physical parameterizations. Recently, the  
82 WRF model has adapted improved convection and boundary layer schemes in the Rapid  
83 Refresh (RAP) model operational at the National Centers for Environmental Prediction (NCEP,  
84 Benjamin et al., 2016). The first question we want to answer in this paper is to what extent  
85 these modifications can improve atmospheric simulations in the Arctic (i.e., radiation,  
86 temperature, humidity, and wind), and then benefit seasonal Arctic sea ice simulation and  
87 prediction. The ROMS model provides several options for tracer advection schemes. These  
88 advection schemes can have different degrees of oscillatory behavior (e.g., Shchepetkin and  
89 McWilliams, 1998). The oscillatory behavior can have impacts on sea ice simulation through  
90 ice-ocean interactions (e.g., Naughten et al., 2017). The second question we want to answer in  
91 this paper is to what extent different advection schemes can change the simulation of upper  
92 ocean thermal structure and then Arctic sea ice prediction. Several recent efforts have  
93 incorporated prognostic salinity into sea ice models. The CICE model has a new mushy-layer  
94 thermodynamics parameterization that includes prognostic salinity and treats sea ice as a two-  
95 phase mushy layer (Turner et al., 2013). Bailey et al. (2020) showed that the mushy-layer  
96 physics has noticeable impacts on Arctic sea ice simulation within the Community Earth  
97 System Model version 2. The third question we want to answer in this paper is whether the  
98 mushy-layer scheme can produce noticeable influence on seasonal Arctic sea ice prediction.

---

99 Currently, SIPN focuses on Arctic sea ice predictions during the melting season, particularly  
100 the seasonal minimum. It is not clear that how predictive skills of dynamical models  
101 participating in SIPN may change for longer period, i.e., extending into the freezing up period,  
102 which also have significance on socioeconomic aspects. The assessment of the skills of global  
103 climate models (GCMs) in predicting Pan-Arctic sea ice extent with suites of hindcasts  
104 suggested that GCMs may have skills at lead times of 1-6 months (e.g., Blanchard-  
105 Wrigglesworth et al., 2015; Chevallier et al., 2013; Guemas et al., 2016; Merryfield et al., 2013;  
106 Msadek et al., 2014; Peterson et al., 2015; Sigmond et al., 2013; Wang et al., 2013; Zampieri  
107 et al., 2018). Moreover, some studies using a “perfect model” approach, which treats one  
108 member of an ensemble as the truth (i.e., assuming the model is perfect without bias) and  
109 analyzes the skill of other members in predicting the response of the “truth” member (e.g.,  
110 Meehl et al., 2007), suggested that Arctic sea ice cover can be potentially predictable up to two  
111 years in advance (e.g., Blanchard-Wrigglesworth et al., 2011; Blanchard-Wrigglesworth and  
112 Bushuk, 2018; Day et al., 2016; Germe et al., 2014; Tietsche et al., 2014). The last question we  
113 want to answer in this paper is whether CAPS has predictive skill for longer periods (up to 7  
114 months).

115 This paper is structured as follows. Section 2 provides a brief overview of CAPS,  
116 including model configurations and data assimilation procedures. Section 3 describes the  
117 designs of the prediction experiments for the year of 2018 based on major improvements/  
118 changes in the model components compared to its predecessor described in Y20, examines the  
119 performance of the updated CAPS, and offers physical links between Arctic sea ice changes

---

120 and improved/changed physical parameterizations. Section 4 discusses the predictive skill of  
121 CAPS at longer timescale. Discussions and concluding remarks are given in section 5.

## 122 **2. Coupled Arctic Prediction System (CAPS)**

123 As described in Y20, CAPS has been developed by coupling the Community Ice Code  
124 (CICE) with the Weather Research and Forecasting Model (WRF) and the Regional Ocean  
125 Modeling System (ROMS) based on the framework of the Coupled Ocean-Atmosphere-Wave-  
126 Sediment Transport (Warner et al., 2010). The general description of each model component in  
127 CAPS is referred to Y20. The advantage of CAPS is its model components have a variety of  
128 physics for us to choose and capability to integrate follow-up improvements of physical  
129 parameterizations. With recent achievements of community efforts, we update CAPS based on  
130 newly-released WRF, ROMS, and CICE models. During this update, we focus on the Rapid  
131 Refresh (RAP) physics in the WRF model, the oceanic tracer advection scheme in the ROMS  
132 model, sea ice thermodynamics in the CICE model (see details in section 3), and investigate  
133 physical processes linking them to Arctic sea ice simulation and prediction. The same physical  
134 parameterizations described in Y20 are used here for the control simulation (see Table 1). Major  
135 changes in physical parameterizations as well as the model infrastructure in the WRF, ROMS,  
136 and CICE models are described in section 3.

137 As described in Y20, the Parallel Data Assimilation Framework (PDAF, Nerger and Hiller,  
138 2013) was implemented in CAPS, which provides a variety of optimized ensemble-based  
139 Kalman filters. The Local Error Subspace Transform Kalman Filter (LESTKF; Nerger et al.,  
140 2012) is used to assimilate satellite-observed sea ice parameters. The LESTKF projects the

---

141 ensemble onto the error subspace and then directly computes the ensemble transformation in  
142 the error subspace. This results in better assimilation performance and higher computational  
143 efficiency compared to the other filters as discussed in Nerger et al. (2012).

144 The initial ensembles are generated by applying the second-order exact sampling (Pham,  
145 2001) to simulated sea ice state vectors (ice concentration and thickness) from an one-month  
146 free run, and then assimilating sea ice observations, including: 1) the near real-time daily Arctic  
147 sea ice concentration processed by the National Aeronautics and Space Administration (NASA)  
148 Team algorithm (Maslanik and Stroeve, 1999) obtained from the NSIDC  
149 (<https://nsidc.org/data/NSIDC-0081/>), and 2) a combined monthly sea ice thickness derived  
150 from the CryoSat-2 (Laxon et al., 2013; obtained from <http://data.seaiceportal.de>), and daily  
151 sea ice thickness derived from the Soil Moisture and Ocean Salinity (SMOS; Kaleschke et al.,  
152 2012; Tian-Kunze et al., 2014; obtained from [https://icdc.cen.uni-hamburg.de/en/l3c-smos-](https://icdc.cen.uni-hamburg.de/en/l3c-smos-sit.html)  
153 [sit.html](https://icdc.cen.uni-hamburg.de/en/l3c-smos-sit.html)). To address the issue that sea ice thickness derived from CyroSat-2 and SMOS are  
154 unavailable during the melting season, the melting season ice thickness is estimated based on  
155 the seasonal cycle of the Pan-Arctic Ice Ocean Modeling and Assimilation System (PIOMAS)  
156 daily sea ice thickness (Zhang and Rothrock, 2003).

157 Different from Y20, in this study, we change the localization radius from 2 to 6 grids  
158 during the assimilation procedures to reduce some instability during initial Arctic sea ice  
159 simulations associated with 2 localization radii. As shown in Supplementary Figure S1, the ice  
160 thickness with 2 localization radii and 1.5 m uncertainty (used in Y20) shows some  
161 discontinuous features (Fig. S1a), which tend to result in numerical instability during the initial



---

162 integration. Such discontinuous features are obviously corrected with 6 localization radii and  
163 0.75 m uncertainty (Fig. S1b). Following Y20, here we test the 2018 prediction experiment  
164 with 6 localization radii for the data assimilation, which shows very similar temporal evolution  
165 of the total Arctic sea ice extent for the July experiment relative to that of Y20, although it (red  
166 solid line) predicts slightly less ice extent than that of Y20 (blue line) (Supplementary Figure  
167 S2). In this study, this configuration is designated as the reference for the following assessment  
168 of the updated CAPS (hereafter Y20\_MOD).

169 For the evaluation of Arctic sea ice prediction, Sea Ice Index (Fetterer et al., 2017;  
170 obtained from <https://nsidc.org/data/G02135>) is used as the observed total sea ice extent, and  
171 the NSIDC sea ice concentrations (SIC) derived from Special Sensor Microwave  
172 Imager/Sounder (SSMIS) with the NASA Team algorithm (Cavalieri et al., 1996; obtained from  
173 <https://nsidc.org/data/nsidc-0051>) is also used. For the assessment of the simulated atmospheric  
174 and oceanic variables, the European Centre for Medium-Range Weather Forecasts (ECMWF)  
175 reanalysis version 5 (ERA5; Hersbach et al., 2020; obtained from  
176 <https://cds.climate.copernicus.eu>) and National Oceanic and Atmospheric Administration  
177 (NOAA) Optimum Interpolation (OI) Sea Surface Temperature (SST) (Reynolds et al., 2007;  
178 obtained from <https://psl.noaa.gov/data/gridded/data.noaa.oisst.v2.highres.html>) are utilized.  
179 For the comparison of spatial distribution, SIC, ERA5, and OISST are interpolated to the model  
180 grid.

### 181 3. Evaluation of updated CAPS

#### 182 3.1. Experiment designs and methodology

---

183 The model domain includes 319 (449) x- (y-) grid points with a ~24 km grid spacing for  
184 all model components (see Figure 2 in Y20). The WRF model uses 50 vertical levels, the  
185 ROMS model uses 40 vertical levels, and the CICE model uses 7 ice layers, 1 snow layer, and  
186 5 categories of sea ice thickness. The coupling frequency across all model components is 30  
187 minutes. Initial and boundary conditions for the WRF and ROMS models are generated from  
188 the Climate Forecast System version 2 (CFSv2, Saha et al., 2014) operational forecast archived  
189 at NCEP (<http://nomads.ncep.noaa.gov/pub/data/nccf/com/cfs/prod/>). Sea ice initial conditions  
190 are generated from the data assimilation described in section 2. Ensemble predictions with 8  
191 members are conducted. A set of numerical experiments for the Pan-Arctic seasonal sea ice  
192 prediction with different physics, starting from July 1<sup>st</sup> to October 1<sup>st</sup> for the year of 2018, has  
193 been conducted. Table 2 provides the details of these experiments that allow us to examine  
194 physical processes linking improved/changed physical parameterizations in the updated CAPS  
195 to Arctic sea ice simulation and prediction.

196 In this study, sea ice extent is calculated as the sum of area of all grid cells with ice  
197 concentration greater than 15%. Besides the total Arctic sea ice extent, we also calculate the  
198 ice extent for the following subregions: 1) Beaufort and Chukchi Seas (120°W-180, 60°N-  
199 80°N), 2) East Siberian and Laptev Seas (90°E-180, 60°N-80°N), and 3) Barents, Kara, and  
200 Greenland Seas (30°W-90°E, 60°N-80°N). To further assess the predictive skill of Arctic sea  
201 ice predictions, we show the climatology prediction (CLIM, the period of 1998-2017) and the  
202 damped anomaly persistence prediction (DAMP). Following Van den Dool (2006), the DAMP  
203 prediction is generated from the initial sea ice extent anomaly (relative to the 1998-2017

---

204 climatology) scaled by the autocorrelation and the ratio of standard deviation between different  
205 lead times and initial times (see the DAMP equation in Y20).

206 In order to understand physical contributors that drive the evolution of Arctic sea ice state  
207 (the standard variables of the ice concentration and thickness), the mass budget of Arctic sea  
208 ice for all experiments is analyzed in this study as defined in Notz et al. (2016, Append. E),  
209 including:

- 210 ● sea ice growth in supercooled open water (frazil)
- 211 ● sea ice growth at the bottom of the ice (basal growth)
- 212 ● sea ice growth due to transformation of snow to sea ice (snowice)
- 213 ● sea ice melt at the air-ice interface (top melt)
- 214 ● sea ice melt at the bottom of the ice (basal melt)
- 215 ● sea ice melt at the sides of the ice (lateral melt)
- 216 ● sea ice mass change due to dynamics-related processes (e.g. advection) (dynamics)

217 These diagnostic variables are determined by saving the ice mass tendency of above  
218 processes separately every time step and integrated to output the daily-mean value.

### 219 **3.2. Impacts of the RAP physics in the WRF model**

220 To examine the performance of the upgrades of physical parameterization in component  
221 models in CAPS one step at a time compared to its predecessor in Y20, we define the  
222 Y21\_CTRL experiment that uses the RAP physics in the WRF model (see Table 2 for  
223 differences between Y21\_CTRL and Y20\_MOD). Recently, the Rapid Refresh (RAP) model,  
224 a high-frequency weather prediction/assimilation modeling system operational at the National

---

225 Centers for Environmental Prediction (NCEP), has made some improvements in the WRF  
226 model physics (Benjamin et al., 2016), including improved Grell-Freitas convection scheme  
227 (GF) and Mellor-Yamada-Nakanishi-Niino planetary boundary layer scheme (MYNN). For the  
228 GF scheme, the major improvements relative to the original scheme (Grell and Freitas, 2014)  
229 include: 1) a beta probability density function used as the normalized mass flux profile for  
230 representing height-dependent entrainment/detrainment rates within statistical-averaged deep  
231 convective plumes, which is given as:

$$244 \quad Z_{u,d}(r_k) = cr_k^\alpha - (1 - r_k)^\beta - 1$$

232 where  $Z_{u,d}$  is the mass flux profiles for updrafts and downdrafts,  $c$  is a normalization constant,  
233  $r_k$  is the location of the mass flux maximum,  $\alpha$  and  $\beta$  determine the skewness of the beta  
234 probability density function, and 2) the ECMWF approach used for momentum transport due  
235 to convection (Biswas et al. 2020; Freitas et al. 2018; 2021). For the MYNN scheme, the RAP  
236 model improves the mixing-length formulation, which is designed as:

$$245 \quad \frac{1}{l_m} = \frac{1}{l_s} + \frac{1}{l_t} + \frac{1}{l_b}$$

237 where  $l_m$  is the mixing length,  $l_s$  is the surface length,  $l_t$  is the turbulent length, and  $l_b$  is  
238 the buoyancy length. Compared to the original scheme, the RAP model changed coefficients  
239 in the formulation of  $l_s$ ,  $l_t$ , and  $l_b$  for reducing the near-surface turbulent mixing, and the  
240 diffusivity of the scheme. The RAP model also removes numerical deficiencies to better  
241 represent subgrid-scale cloudiness (Benjamin et al. 2016, see Append. B) compared to the  
242 original scheme (Nakanishi and Nino, 2009). In addition, some minor issues in the Noah land  
243 surface model (Chen and Dudhia, 2001) have been fixed, including discontinuous behavior for

---

246 soil ice melting, negative moisture fluxes over glacial, and associated with snow melting.

247       Apparently, the above RAP physics can have influence on the behavior of simulated  
248 atmospheric thermodynamics (i.e., radiation, temperature). Figure 1 and 2 show the spatial  
249 distribution of the ERA5 surface downward solar and thermal radiation (SWDN and LWDN),  
250 the prediction errors (ensemble mean minuses ERA5) of Y20\_MOD, and the difference  
251 between Y21\_CTRL and Y20\_MOD. For July, Y20\_MOD (Fig. 1d) results in less SWDN over  
252 most of ocean basins as well as Alaska and northeast US, western Siberia, and eastern Europe,  
253 but more SWDN over southern and eastern Siberia compared with ERA5. For August and  
254 September (Fig. 1e-f), the spatial distribution is generally similar to that of July, except that  
255 eastern Siberia (less SWDN) and northern Canada (more SWDN) in August. It appears that the  
256 magnitude of the prediction errors tends to decrease over the areas with large prediction errors  
257 as the prediction time increases (i.e., July vs. September). Compared with Y20\_MOD, the RAP  
258 physics in Y21\_CTRL results in large areas with smaller prediction errors in July (e.g., the  
259 positive difference between Y21\_CTRL and Y20\_MOD reduces the negative prediction errors  
260 in Y20\_MOD), except the north Pacific (especially the Sea of Okhotsk) and north Canada (Fig.  
261 1g). For August and September (Fig. 1h, i), encouragingly, there are more areas with smaller  
262 prediction errors.

263       In contrast to SWDN, the prediction errors of LWDN in Y20\_MOD have much smaller  
264 magnitude (up to 100 W/m<sup>2</sup> in SWDN vs. 50 W/m<sup>2</sup> in LWDN) for the entire prediction period  
265 (Fig. 2d-f). For July, Y20\_MOD (Fig. 2d) simulates less LDWN over most of the model domain  
266 compared with ERA5, except the Atlantic sector and north Greenland. For August, the areas

---

267 with negative prediction errors expand and the magnitude of prediction errors increases  
268 (particularly in southeastern Siberia and northeast US) compared to that of July (Fig. 2e). For  
269 September (Fig. 2f), the spatial distribution of LWDN is mostly similar to that of July, except  
270 that north Canada and Canadian Archipelago show positive prediction errors. The Y21\_CTRL  
271 experiment with the RAP physics tends to reduce the prediction errors in Y20\_MOD, especially  
272 over eastern Siberia and the Atlantic sector in July to September (Fig. 2g-i). However,  
273 Y21\_CTRL results in larger bias in the central Northern Atlantic in August than that of  
274 Y20\_MOD (Fig. 2h).

275 Figure 3 shows the spatial distribution of the ERA5 2m air temperature, the prediction  
276 errors of Y20\_MOD, and the difference between Y21\_CTRL and Y20\_MOD. For Y20\_MOD,  
277 the predicted air temperature in July has small cold prediction errors over all ocean basins,  
278 small-to-moderate cold prediction errors (~3-5 degrees) over Canada and Siberia, and  
279 moderate-to-large cold prediction errors (~6-9 degrees) over eastern Europe (Fig. 3d). In  
280 August (Fig. 3e), the cold prediction errors over most of the model domain are increased, in  
281 particular, very large cold prediction error (over 10 degrees) is located over east Siberia. In  
282 September, these cold prediction errors are decreased relatively, and some warm prediction  
283 errors are found in north of Greenland (Fig. 3f). With the adaptation of the RAP physics in the  
284 WRF model, Y21\_CTRL, in general, produces a warmer state in most of the model domain  
285 compared to that of Y20\_MOD during the entire prediction period. For July (Fig. 3g), the  
286 predicted air temperature is slightly warmer over the Arctic Ocean, the Pacific, and Atlantic  
287 sectors, moderately warmer (~1-2 degrees) over central and eastern Siberia and Canadian

---

288 Archipelago, but the slightly colder over northern Canada than that of Y20\_MOD. For August  
289 and September (Fig. 3h), most of the model domain is warmer in Y21\_CTRL than that of  
290 Y20\_MOD, in particular excessive cold prediction errors shown in Y20\_MOD over Siberia are  
291 reduced notably ( $\sim 2.5$ -4 degrees). We notice that the RAP physics does not have significant  
292 impacts on atmospheric circulations, given that Y21\_CTRL and Y20\_MOD have very similar  
293 wind patterns (not shown).

294 Figure 4 shows the temporal evolution of the ensemble mean of the predicted Arctic sea  
295 ice extent along with the NSIDC observations. In terms of total ice extent, compared to the  
296 Y20\_MOD experiment (blue line), the Y21\_CTRL experiment (yellow line) produces  $\sim 0.5$   
297 million  $\text{km}^2$  more ice extent at the initial. Note that the difference in the initial ice extent is  
298 related to that sea ice fields in Y20\_MOD and Y21\_CTRL (as well as other experiments listed  
299 in Table 2) are initialized based on one-month free runs (section 2), which use different physical  
300 configurations listed in Table 2. These one-month free runs do not have the same evolution in  
301 sea ice fields and result in different initial ice fields after data assimilation. The ice extent in  
302 Y21\_CTRL decreases faster than Y20\_MOD during the first 2-week integration. After that,  
303 they track each other closely, and predict nearly the same minimum ice extent ( $\sim 4.3$  million  
304  $\text{km}^2$ ). Like Y20\_MOD, Y21\_CTRL still has a delayed ice recovery in late September compared  
305 to the observations. Compared with the CLIM/DAMP predictions (black dashed and dotted  
306 lines), both Y20\_MOD and Y21\_CTRL have smaller prediction errors in August, but  
307 comparable prediction errors after early September.

308 The difference in sea ice extent becomes larger at regional scales, in the East Siberian-

---

309 Laptev Seas, Y21\_CTRL shows faster ice decline after mid-July than that of Y20\_MOD,  
310 whereas in the Beaufort-Chukchi Seas, Y21\_CTRL predicts slower ice retreat after late July  
311 than that of Y20\_MOD (Fig. 4a, 4b). They are consistent with that Y21\_CTRL predicts warmer  
312 (relatively colder) temperature than that of Y20\_MOD in the East Siberian-Laptev (Beaufort-  
313 Chukchi) Seas. Both Y20\_MOD and Y21\_CTRL agree well with the observations in the  
314 Barents-Kara-Greenland Seas (Fig. 4c). Compared with the observations, Y20\_MOD performs  
315 relatively better in regional ice extents than that of Y21\_CTRL. Figure 5 shows the spatial  
316 distribution of the NSIDC sea ice concentration and the difference between the predicted ice  
317 concentration and the observations for all grid cells that the predictions and the observations  
318 both have at least 15% ice concentration. The vertical and horizontal lining areas represent  
319 difference of the ice edge location. Like regional ice extent shown in Figure 4, Y21\_CTRL  
320 predicts lower (higher) ice concentration along the East Siberian-Laptev (Beaufort-Chukchi)  
321 Seas (Fig. 5e<sub>1</sub>-e<sub>3</sub>). Y21\_CTRL also predicts less ice in the central Arctic Ocean in August and  
322 September, which is consistent with warmer temperature in Y21\_CTRL relative to Y20\_MOD.

323 Figure 6 shows the evolution of sea ice mass budget terms of Y20\_MOD and Y21\_CTRL,  
324 averaged with cell-area weighting over the entire model domain. During the entire prediction  
325 period, most of the ice loss in Y20\_MOD and Y21\_CTRL are caused by basal melting. The  
326 surface melting has relatively small contribution in the total ice loss and mainly occurs in July.  
327 However, compared with Y20\_MOD (Fig. 6a), Y21\_CTRL (Fig. 6b) shows much larger  
328 magnitude for basal and surface melt. In a fully coupled predictive model, the changes of sea  
329 ice are determined by the fluxes from the atmosphere above and the ocean below. Associated



---

330 with the increased downward radiation of the above RAP physics, Y21\_CTRL absorbs more  
331 shortwave radiation (SWABS, Fig. 7a) and allows more penetrating solar radiation into the  
332 upper ocean below sea ice (SWTHRU, Fig. 7b) than that of Y20\_MOD, especially in July. This  
333 explains why Y21\_CTRL has larger magnitude of surface and basal melting terms. Although  
334 Y21\_CTRL show larger magnitude in surface and basal melting than that of Y20\_MOD, the  
335 ice extent in Y21\_CTRL and Y20\_MOD shown in Figure 4 show similar evolution. The effect  
336 of larger surface and basal melting in Y21\_CTRL is largely reflected in the ice thickness change.  
337 As shown in Figure S3, Y21\_CTRL has thinner ice thickness than that of Y20\_MOD, in the  
338 East Siberian-Laptev Seas in July and in the much of central Arctic Ocean in August and  
339 September.

340

### 341 3.3. Impacts of the tracer advection in ROMS model

342 Currently, the ROMS model that uses a generalized topography-following coordinate has  
343 two vertical coordinate transformation options:

$$348 \quad z(x, y, \sigma, t) = S(x, y, \sigma) + \zeta(x, y, t) \left[ 1 + \frac{S(x, y, \sigma)}{h(x, y)} \right] \quad (1)$$

$$S(x, y, \sigma) = h_c \sigma + [h(x, y) - h_c] C(\sigma)$$

344 or

$$349 \quad z(x, y, \sigma, t) = \zeta(x, y, t) + [\zeta(x, y, t) + h(x, y)] S(x, y, \sigma)$$

$$S(x, y, \sigma) = \frac{h_c \sigma + h(x, y) C(\sigma)}{h_c + h(x, y)} \quad (2)$$

345 where  $S(x, y, \sigma)$  is a nonlinear vertical transformation function,  $\zeta(x, y, t)$  is the free-surface,  
346  $h(x, y)$  is the unperturbed water column thickness,  $C(\sigma)$  is the non-dimensional, monotonic,  
347 vertical stretching function, and  $h_c$  controls the behavior of the vertical stretching. In Y20, we

---

350 used the transformation 1 and the vertical stretching function introduced by Song and  
351 Haidvogel (1994). However, the vertical transformation 1 has an inherent limitation for the  
352 value of  $h_c$  (expected to be the thermocline depth), which must be less than or equal to the  
353 minimum value in  $h(x, y)$ . As a result,  $h_c$  was chosen as 10 meters due to the limitation of  
354 the minimum value in  $h(x, y)$  in Y20. This limitation is removed with the vertical  
355 transformation 2 and  $h_c$  can be any positive value. Here the Y21\_VT experiment is conducted  
356 to examine the impact of the vertical transformation in the ROMS model on seasonal Arctic  
357 sea ice simulation and prediction, which uses the vertical transformation 2, the Shchepetkin  
358 vertical stretching function (a function introduced in a research version of ROMS at University  
359 of California, Los Angeles), and 300 meters for  $h_c$ . As shown in Supplementary Figure S4-S5,  
360 compared to Y21\_CTRL, Y21\_VT is less sensitive to the bathymetry and its layers are more  
361 evenly-distributed in the upper 300 meters. With the changes of vertical layers of the upper  
362 ocean, the Y21\_VT experiment has minor SST changes relative to Y21\_CTRL. The simulated  
363 temporal evolution of total ice extent of Y21\_VT (Fig. 4, red line) resembles to that of  
364 Y21\_CTRL (Fig. 4, yellow line), although some differences are seen at the regional scale in  
365 the areas with shallow water (e.g., East Siberian, Laptev, Barents, and Kara Seas). The  
366 configuration of Y21\_VT is used in the following experiments.

367 It has been recognized that the tracer advection and the vertical mixing schemes have  
368 important effects on ocean and sea ice simulation (e.g., Liang and Losch, 2018; Naughten et  
369 al., 2017). Here the Y21\_RP experiment is designated to explore the influence of different  
370 advection schemes in the ROMS model. Specifically, the tracer advection scheme is changed

---

371 from the Multidimensional positive definite advection transport algorithm (MPDATA;  
372 Smolarkiewicz, 2006) to the third-order upwind horizontal advection (U3H; Rasch, 1994;  
373 Shchepetkin, and McWilliams, 2005) and the fourth-order centered vertical advection schemes  
374 (C4V; Shchepetkin, and McWilliams, 1998; 2005). The MPDATA scheme applied in  
375 Y20\_MOD, Y21\_CTRL, and Y21\_VT is a non-oscillatory scheme but a sign preserving  
376 scheme (Smolarkiewicz, 2006). This means MPDATA is not suitable for tracer fields having  
377 both positive and negative values (i.e., temperature with degree Celsius in the ROMS model).  
378 The upwind third-order (U3H) scheme used in Y21\_RP is an oscillatory scheme but it  
379 significantly reduces oscillations compared to other centered schemes (e.g., Hecht et al., 2000;  
380 Naughten et al., 2017) available in the ROMS model.

381 Figure 8 shows the spatial distribution of the SST changes of Y21\_VT and Y21\_RP  
382 relative to Y21\_CTRL (as well as the OISST and the difference between Y21\_CTRL and  
383 OISST). In general, Y21\_CTRL shows cold prediction errors in the North Pacific (~2 degrees)  
384 and the Atlantic (~3 degrees) compared to that of OISST in July, and these cold prediction  
385 errors are enhanced as the prediction time increases (to 3-5 degrees, Fig. 8d-f). With the  
386 U3H/C4V tracer advection scheme in Y21\_RP, cold prediction errors shown in Y21\_CTRL are  
387 reduced significantly in the north Pacific and Atlantic, but SST under sea ice in much of the  
388 Arctic Ocean is slightly colder than that of Y21\_CTRL (Fig. 8j-l).

389 Y21\_RP (Fig. 4, green line) shows comparable temporal evolution of the ice extent as  
390 Y21\_CTRL (as well as Y21\_VT) until near the end of July. After that, the ice melting slows  
391 down (closer to the observations) and the ice extent begins to recover earlier (after the first

---

392 week of September) in Y21\_RP compared to that of Y21\_CTRL. This leads to much smaller  
393 prediction error in seasonal minimum ice extent relative to the observation. Y21\_RP also shows  
394 better predictive skill after late August compared with the CLIM/DAMP predictions (black  
395 dashed and dotted lines). This suggests the delayed ice recovery in late September shown in  
396 Y20\_MOD, Y21\_CTRL and Y21\_VT is in part due to the choice of ocean advection and  
397 vertical mixing schemes, which change the behavior of ocean state. At the regional scale, the  
398 slower ice decline after July and earlier recovery of the ice extent in September mainly occur  
399 in the Beaufort-Chukchi and Barents-Kara-Greenland Seas compared to that of Y21\_CTRL  
400 (Fig. 4a, c). With U3H/C4V scheme, the Y21\_RP experiment simulates higher sea ice  
401 concentration than that of Y21\_VT (Fig. 5f<sub>1</sub>-f<sub>3</sub>). For September, the Y21\_RP experiment better  
402 predicts the ice edge location in the Atlantic sector of the Arctic (i.e., smaller areas with  
403 horizontal/vertical lining) compared to the experiments described above (not shown).

404 Figure 9 shows the evolution of sea ice mass budget terms of Y21\_VT and Y21\_RP.  
405 Relative to Y21\_VT, Y21\_RP (with U3H/C4V scheme) results in increased frazil ice formation  
406 in July, which is partly compensated by increased surface melting. Y21\_RP also leads to  
407 increased basal growth in mid- and late September (Fig. 9a, b).

408 Figure 10 shows the difference in the vertical profile of ocean temperature and salinity in  
409 the upper 150 m averaged for the central Arctic Ocean between Y21\_RP and Y21\_VT. The  
410 ocean temperature in the surface layer of Y21\_RP is slightly colder during the prediction period  
411 compared to that of Y21\_VT (Fig. 10a), especially in August and September. Moreover, the  
412 water in the surface layer (0-20 m) of Y21\_RP is fresher than that of Y21\_VT (Fig. 10b). It

---

413 reduces the freezing temperature and favors frazil ice formation. In CAPS, frazil ice formation  
414 is determined by the freezing potential, which is the vertical integral of the difference between  
415 temperature in upper ocean layer and the freezing temperature in the upper 5 m-layer. The  
416 temperature of supercooled water is adjusted based on the freezing potential to form new ice  
417 and rejects brine into the ocean that leads to saltier water between 20-50 m in Figure 10. It  
418 should be noted that the increased frazil ice formation in July in Y21\_RP might be also the  
419 results of model adjustment and/or numerical error. The oscillatory behavior of U3H scheme  
420 can make the temperature fall below the freezing point and then instantaneously forms new ice  
421 (as well as temperature/salinity adjustments).

#### 422 **3.4. Impacts of sea ice thermodynamics in the CICE model**

423 In Y20, we used sea ice thermodynamics introduced by Bitz and Lipscomb (1999;  
424 hereafter BL99) as the setup of CAPS, which assumes a fixed vertical salinity profile based on  
425 observations. The new CICE model includes a MUSHY-layer ice thermodynamics introduced  
426 by Turner et al. (2013), which simulates vertically and time-varying prognostic salinity and  
427 associated effects on thermodynamic properties of sea ice. In the Y21\_MUSHY experiment,  
428 we change the ice thermodynamics from BL99 to MUSHY (Table 2) to examine whether  
429 improved ice thermodynamics has noticeable influence on Arctic sea ice simulation and  
430 prediction at seasonal timescale. Compared to Y21\_RP, Y21\_MUSHY (Fig. 4, pink line)  
431 produces very similar evolution of total ice extent. However, it simulates relatively larger ice  
432 extent near the end of September, which is also reflected by the basin-wide increased ice cover  
433 shown in Figure 5h<sub>3</sub>. At the regional scale, compared to Y21\_RP, Y21\_MUSHY predicts less

---

434 ice in August in the Beaufort-Chukchi. The opposite is the case for the East Siberian-Laptev  
435 Seas (Fig. 4a, b).

436 Figure 11 shows the difference of the ensemble mean of the predicted ice thickness  
437 between Y21\_MUSHY and Y21\_RP. Compared with Y21\_RP, Y21\_MUSHY simulates  
438 thicker ice (from  $\sim 0.2\text{m}$  in July to over  $0.4\text{m}$  in September) extending from the Canadian Arctic,  
439 through the central Arctic Ocean, to the Laptev Sea (Fig. 11a-c). This seems to be consistent  
440 with previous studies, which show that the Mushy-layer thermodynamics simulates thicker ice  
441 than BL99 thermodynamics in both standalone CICE (Turner and Hunke, 2015) and the fully-  
442 coupled (Bailey et al., 2020), but Y21\_MUSHY shows thinner ice ( $\sim 0.2\text{m}$ ) in an arc extending  
443 from north of Alaska to north of eastern Siberia compared to Bailey et al. (2020). Note that  
444 Y21\_MUSHY focuses the effects of Mushy-thermodynamics on seasonal timescale while the  
445 results in Bailey et al. (2020) are based on 50-year simulations.

446 Compared to Y21\_RP, the mass budget of Y21\_MUSHY (Fig. S6) shows that both surface  
447 melting and frazil ice formation terms are increased. This compensation between surface  
448 melting and frazil ice formation from the Mushy-layer thermodynamics in CAPS leads to  
449 relatively unchanged total ice extent between Y21\_MUSHY and Y21\_RP (Fig. 4 green and  
450 pink lines).

451

#### 452 **4. Prediction skill of CAPS at longer timescale**

453 The design of Arctic sea ice prediction experiments described above follow the protocol  
454 of the Sea Ice Prediction Network (SIPN), in which the outlook start from June 1<sup>st</sup>, July 1<sup>st</sup>, and

---

455 August 1<sup>st</sup> to predict seasonal minimum of the ice extent in September. It is not clear that how  
456 predictive skills of dynamical models participating in SIPN may change for longer period. Here  
457 we conduct two more experiments to investigate the predictive capability of CAPS beyond the  
458 SIPN prediction period. For the prediction experiments discussed above, we use a simple  
459 approach to merge CryoSat-2 and SMOS ice thickness by replacing ice thickness less than 1m  
460 in CryoSat-2 data with SMOS data for ice thickness assimilation. Ricker et al. (2017) presented  
461 a new ice thickness product (CS2SMOS) based on the optimal interpolation to statistically  
462 merge CryoSat-2 and SMOS data. Here we utilize the configuration of Y21\_RP but use  
463 CS2SMOS SIT for the assimilation (Y21\_SIT; Table 2). The predicted total ice extent is almost  
464 identical to Y21\_RP in July but slightly larger total extent after July than that of Y21\_RP (not  
465 shown). The configuration of Y21\_SIT is used in the following experiments. Taking advantage  
466 of the entire prediction period provided by CFS forecasts (7 months), the Y21\_EXT-7  
467 experiment is designed to extend the prediction period to the end of January next year (Table  
468 2). Figure 12 shows the temporal evolution of the ensemble mean of the predicted total Arctic  
469 sea ice extent (as well as regional ice extent) for Y21\_EXT-7. Total ice extent of Y21\_EXT-7  
470 exhibits reasonable evolution in terms of seasonal minimum and timing of recovery compared  
471 with the observations until late November. Y21\_EXT-7 also performs better than that of the  
472 CLIM/DAMP predictions (black dashed and dotted lines) until mid-to-late November. After  
473 that, Y21\_EXT-7 overestimates total ice extent relative to the observations, and such  
474 overestimation is largely contributed by more extensive sea ice in the Barents-Kara-Greenland  
475 Seas (Fig. 12c), which is a result of a sharp increase in the basal growth term after mid-to-late

---

476 November (not shown).

## 477 **5. Conclusions and Discussions**

478 This paper presents and evaluates the updated Coupled Arctic Prediction System (CAPS)  
479 designated for Arctic sea ice prediction through a case study for the year of 2018. A set of Pan-  
480 Arctic prediction experiments with improved/changed physical parameterizations as well as  
481 different configurations starting from July 1<sup>st</sup> to the end of September are performed for 2018  
482 to assess their impacts of the updated CAPS on the predictive skill of Arctic sea ice at seasonal  
483 timescale. Specifically, we focus on the Rapid Refresh (RAP) physics in the WRF model, the  
484 oceanic tracer advection scheme in the ROMS model, sea ice thermodynamics in the CICE  
485 model, and investigate physical processes linking them to Arctic sea ice simulation and  
486 prediction.

487 The results show that the updated CAPS with improved physical parameterizations can  
488 better predict the evolution of total ice extent compared with its predecessor described in Yang  
489 et al. (2020), though the predictions exhibit some prediction errors in regional ice extent. The  
490 key improvements of WRF, including cumulus, boundary layer, and land surface schemes,  
491 result in improved simulations in downward radiative fluxes and near surface air temperature.  
492 These improvements mainly influence the predicted ice thickness instead of total ice extent.  
493 The difference in the predicted ice thickness can have potential impacts on the icebreakers  
494 planning their routes across the ice-covered regions. The major changes of ROMS, including  
495 tracer advection and vertical mixing schemes, reduces the prediction errors in sea surface  
496 temperature and changes ocean temperature and salinity structure in the surface layer, leading



---

497 to improved evolution of the predicted total ice extent (particularly correcting the late ice  
498 recovery issue in the previous CAPS). The changes of CICE, including improved ice  
499 thermodynamics, have noticeable influences on the predicted ice thickness.

500 We demonstrate that CAPS can remain skillful beyond the designated period of Sea Ice  
501 Prediction Network (SIPN), which has potential values for stakeholders to make decisions  
502 regarding the socioeconomical activities in the Arctic. Although CAPS shows extended  
503 predictive skill to the freeze-up period, the prediction produces extensive ice through the basal  
504 growth near the end of prediction. The excessive basal growth may be partly due to that the  
505 bias of the CFS data propagates into the model domain through lateral boundary conditions  
506 and its accumulated effect influences Arctic sea ice simulation during the freeze-up period.

507 Keen et al. (2021) analyzed the Arctic mass budget of 15 models participated in the  
508 Coupled Model Intercomparison Project Phase 6 (CMIP6). We notice that, first, the top melting  
509 and the basal melting terms in CMIP6 models have comparable contributions in July while the  
510 top melting term only has ~50% contribution relative to the basal melting term in CAPS. The  
511 updated CAPS with the RAP physics improves the performance of shortwave/longwave  
512 radiation at the surface (Fig. 1 and Fig. 2). The net flux at the ice surface, however, may still  
513 be underestimated in the updated CAPS. Besides, the surface property of sea ice (i.e., the  
514 amount of melt ponds, bare ice, and snow) is a factor that influences surface albedo and thus  
515 the absorbed shortwave radiation (e.g., Nicolaus et al., 2012; Nicolaus and Katlein, 2013). The  
516 prediction experiments starting at July 1<sup>st</sup> in this study do not consider the initialization of melt  
517 ponds (i.e., zero melt pond coverage at the initial). However, melt ponds start to develop in

---

518 early May based on the satellite observations (e.g., Liu et al., 2015, Fig. 1). The initialization  
519 of melt pond based on the observations (e.g., Ding et al., 2020) in CAPS is a direction to  
520 improve the representation of the ice surface properties. Second, the mass budget analysis by  
521 both Keen et al. (2021) and this study show that the contribution of lateral melting term is  
522 relatively small, which might be due to that CMIP6 models and CAPS assume constant floe-  
523 size (i.e., 300 meters in CICE), which is a critical value to determine the strength of lateral  
524 melting (e.g., Horvat et al., 2016; Steele, 1992). Recently, several studies have proposed floe  
525 size distribution models (e.g., Bateson et al., 2020; Bennetts et al., 2017; Boutin et al., 2020;  
526 Horvat and Tziperman, 2015; Roach et al., 2018, 2019; Zhang et al., 2015, 2016). Incorporating  
527 floe size distribution model in CAPS and understanding its impacts on seasonal Arctic sea ice  
528 prediction will be a future direction of developing CAPS. Lastly, the prediction experiments  
529 with the upwind advection scheme (i.e., Y21\_RP, Y21\_EXT-7) shows spurious large frazil ice  
530 formation, particularly in July, which is different from the analysis shown in Keen et al. (2021).  
531 An approach for reducing spurious frazil ice formation is proposed by Naughten et al. (2017)  
532 that they implemented upwind flux limiter (Leonard and Mokhtari, 1990) to the U3H scheme  
533 to further reduce the oscillations. Naughten et al. (2018) also suggested that the oscillatory  
534 behaviors can be smoothed out by applying the Akima fourth-order tracer advection scheme  
535 combined with Laplacian horizontal diffusion at a level strong enough. Beside of the oscillatory  
536 behaviors of advection scheme, the ice-ocean heat flux may also play a role in the spurious  
537 frazil ice formation. As discussed in section 3.3, the freezing/melting potential not only  
538 determines the amount of newly-formed ice, but also limits the amount of energy that can be

---

539 extracted from the ocean surface layer to melt sea ice. This implies that the ocean surface layer  
540 will be close to the freezing temperature if the ice-ocean heat fluxes reach the limit imposed by  
541 the melting potential. Shi et al. (2021) discussed the impacts of different ice-ocean heat flux  
542 parametrizations on sea ice simulations. Their results suggest that Arctic sea ice will be thicker  
543 and ocean temperature will warmer beneath high-concentration ice with a complex approach  
544 proposed by Schmidt et al. (2004) that limits melt rates (heat fluxes) of sea ice through  
545 considering a fresh water layer underlying sea ice. The warmer ocean temperature under sea  
546 ice with a more complex approach in parameterizing ice-ocean heat flux may be the solution  
547 to reduce the occurrence of local temperature falling below freezing temperature with  
548 oscillatory advection schemes.

549       Based on the prediction experiments discussed in this paper, the configuration with the  
550 RAP physics, the U3H/C4V ocean advection, BL99 ice thermodynamics, and CS2SMOS ice  
551 thickness assimilation (Table 2, Y21\_SIT) is assigned as the finalized CAPS version 1.0.  
552 Improving the representation of physical processes in CAPS version 1.0 for further reducing  
553 the model bias will remain the main focus for the development of CAPS. Since CAPS is a  
554 regional modeling system, it relies on the forecasts from global climate models as initial and  
555 lateral boundary conditions. That is, biases existed in GCM simulations (here the CFS forecast)  
556 can be propagated into and affect the entire area-limited domain (e.g., Bruyère et al., 2014;  
557 Rocheta et al., 2020; Wu et al., 2005). This issue can be a potential source that influences the  
558 predictive capability of CAPS for longer timescales. Studies have applied bias correction  
559 techniques with different complexities for improving the performance of regional modeling

---

560 system (e.g., Bruyère et al., 2014; Colette et al., 2012; Rocheta et al., 2017, 2020). Further  
561 investigation is needed to address biases inherited from GCM predictions through lateral  
562 boundaries for improving the predictive capability of CAPS.  
563

---

564 Code and data availability: The COAWST and CICE models are open source and can be  
565 downloaded from their developers at <https://github.com/jcwarner-usgs/COAWST> and  
566 <https://github.com/CICE-Consortium/CICE>, respectively. PDAF can be obtained from  
567 <https://pdaf.awi.de/trac/wiki>. CAPS v1.0 described in this paper is permanently archived at  
568 <https://doi.org/10.5281/zenodo.5842668>. The prediction data analyzed in this paper can be  
569 accessed from <https://doi.org/10.5281/zenodo.5839510>.

570

571 Author contributions: CYY and JL designed the model experiments, developed the  
572 updated CAPS model, and wrote the manuscript, CYY conducted the prediction experiments  
573 and analyzed the results. DC provided constructive feedback on the manuscript.

574

575 Competing interests: The authors declare that they have no conflict of interest.

576

577 Acknowledgements: This research is supported by the National Key R&D Program of  
578 China (2018YFA0605901), the National Natural Science Foundation of China (42006188 and  
579 41922044), and the Innovation Group Project of Southern Marine Science and  
580 Engineering Guangdong Laboratory (Zhuhai) (311021008). The authors also acknowledge the  
581 National Centers for Environmental Prediction for providing CFS seasonal forecasts, the  
582 University of Hamburg for distributing the SMOS sea ice thickness data, the Alfred-Wegener-  
583 Institut, Helmholtz Zentrum für Polar- und Meeresforschung for providing the CryoSat-2 sea  
584 ice thickness data and CS2SMOS data, the Polar Science Center for distributing the PIOMAS  
585 ice thickness data, the National Snow and Ice Data Center for providing the SSMIS sea ice  
586 concentration data, the European Centre for Medium-Range Weather Forecasts for distributing  
587 the ERA5 reanalysis, and the National Oceanic and Atmospheric Administration for providing  
588 the OI sea surface temperature. The authors thank the editor Qiang Wang and two anonymous

---

589 reviewers for their helpful and constructive comments on the manuscript.

---

590 **6. References**

- 591 Aagaard, K.: A synthesis of the Arctic Ocean circulation. *Rapp. P.-V. Reun.- Cons. Int. Explor.*  
592 *Mer*, 188, 11–22, 1989.
- 593 Bailey, D. A., Holland, M. M., DuVivier, A. K., Hunke, E. C., and Turner, A. K.: Impact of a  
594 new sea ice thermodynamic formulation in the CESM2 sea ice component. *Journal of*  
595 *Advances in Modeling Earth Systems*, 12, e2020MS002154.  
596 <https://doi.org/10.1029/2020MS002154>, 2020.
- 597 Bateson, A. W., Feltham, D. L., Schröder, D., Hosekova, L., Ridley, J. K., and Aksenov, Y.:  
598 Impact of sea ice floe size distribution on seasonal fragmentation and melt of Arctic sea  
599 ice, *The Cryosphere*, 14, 403–428, <https://doi.org/10.5194/tc-14-403-2020>, 2020.
- 600 Bitz, C. M. and Lipscomb, W. H.: An energy-conserving thermodynamic sea ice model for  
601 climate study. *J. Geophys. Res.-Oceans*, 104, 15669–15677, 1999.
- 602 Benjamin, S. G., Weygandt, S. S., Brown, J. M., Hu, M., Alexander, C. R., Smirnova, T. G.  
603 and Manikin, G. S.: A North American hourly assimilation and model forecast cycle: the  
604 Rapid Refresh. *Monthly Weather Review*, 144, 1669–1694.  
605 <https://doi.org/10.1175/MWR-D-15-0242.1>, 2016.
- 606 Bennetts, L. G., O'Farrell, S., and Uotila, P.: Brief communication: Impacts of ocean-wave-  
607 induced breakup of Antarctic sea ice via thermodynamics in a stand-alone version of the  
608 CICE sea-ice model, *The Cryosphere*, 11, 1035–1040, [https://doi.org/10.5194/tc-11-](https://doi.org/10.5194/tc-11-1035-2017)  
609 [1035-2017](https://doi.org/10.5194/tc-11-1035-2017), 2017.
- 610 Biswas, M. K., Zhang, J. A., Grell, E., Kalina, E., Newman, K., Bernardet, L., Carson, L.,  
611 Frimel, J., and Grell, G.: Evaluation of the Grell–Freitas Convective Scheme in the  
612 Hurricane Weather Research and Forecasting (HWRF) Model, *Weather and Forecasting*,  
613 35(3), 1017–1033, 2020.
- 614 Blanchard-Wrigglesworth, E., Bitz, C., and Holland, M.: Influence of initial conditions and  
615 climate forcing on predicting Arctic sea ice. *Geophysical Research Letters*, 38, L18503.  
616 <https://doi.org/10.1029/2011GL048807>, 2011.

---

617 Blanchard-Wrigglesworth, E., and Bushuk, M.: Robustness of Arctic sea-ice predictability in  
618 GCMs. *Climate Dynamics*, 52, 5555–5566, 2018.

619 Blanchard-Wrigglesworth, E., Cullather, R., Wang, W., Zhang, J., and Bitz, C. M.: Model  
620 forecast skill and sensitivity to initial conditions in the seasonal sea ice outlook.  
621 *Geophysical Research Letters*, 42, 8042–8048. <https://doi.org/10.1002/2015GL065860>,  
622 2015.

623 Boutin, G., Lique, C., Ardhuin, F., Rousset, C., Talandier, C., Accensi, M., and Girard-Ardhuin,  
624 F.: Towards a coupled model to investigate wave–sea ice interactions in the Arctic  
625 marginal ice zone, *The Cryosphere*, 14, 709–735, [https://doi.org/10.5194/tc-14-709-](https://doi.org/10.5194/tc-14-709-2020)  
626 2020, 2020.

627 Briegleb, B. P. and Light, B.: A Delta-Eddington multiple scattering parameterization for solar  
628 radiation in the sea ice component of the Community Climate System Model. NCAR  
629 Tech. Note NCAR/TN-472+STR, National Center for Atmospheric Research, 2007.

630 Bruyère, C. L., Done, J. M., Holland, G. J., and Fredrick, S.: Bias corrections of global models  
631 for regional climate simulations of high-impact weather. *Clim Dyn* 43, 1847–1856  
632 (2014). <https://doi.org/10.1007/s00382-013-2011-6>, 2014.

633 Carmack, E., Polyakov, I., Padman, L., Fer, I., Hunke, E., Hutchings, J., Jackson, J., Kelley,  
634 D., Kwok, R., Layton, C., Melling, H., Perovich, D., Persson, O., Ruddick, B.,  
635 Timmermans, M.-L., Toole, J., Ross, T., Vavrus, S., and Winsor, P.: Toward Quantifying  
636 the Increasing Role of Oceanic Heat in Sea Ice Loss in the New Arctic. *Bulletin of the*  
637 *American Meteorological Society* 96, 12, 2079–2105, [https://doi.org/10.1175/BAMS-D-](https://doi.org/10.1175/BAMS-D-13-00177.1)  
638 [13-00177.1](https://doi.org/10.1175/BAMS-D-13-00177.1), 2015.

639 Cavalieri, D. J., Parkinson, C. L., Gloersen, P., and Zwally, H. J.: updated yearly. Sea Ice  
640 Concentrations from Nimbus-7 SMMR and DMSP SSM/I-SSMIS Passive Microwave  
641 Data, Version 1. Boulder, Colorado USA. NASA National Snow and Ice Data Center  
642 Distributed Active Archive Center. <https://doi.org/10.5067/8GQ8LZQVLOVL>, 1996.



---

643 Chen, F. and Dudhia, J.: Coupling an advanced land surface–hydrology model with the Penn  
644 State–NCAR MM5 modeling system. Part I: Model implementation and sensitivity. *Mon.*  
645 *Wea. Rev.*, 129, 569–585, 2001.

646 Chevallier, M., Salas y Mélia, D., Voldoire, A., Déqué, M., and Garric, G.: Seasonal forecasts  
647 of the pan-Arctic sea ice extent using a GCM-based seasonal prediction system. *Journal*  
648 *of Climate*, 26(16), 6092–6104, 2013.

649 Colette, A., Vautard, R., and Vrac, M.: Regional climate downscaling with prior statistical  
650 correction of the global climate forcing, *Geophys. Res. Lett.*, 39, L13707,  
651 <https://doi.org/10.1029/2012GL052258>, 2012.

652 Day, J. J., Tietsche, S., Collins, M., Goessling, H. F., Guemas, V., Guillory, A., et al.: The  
653 Arctic predictability and prediction on seasonal-to-interannual timescales (apposite) data  
654 set version 1. *Geoscientific Model Development*, 9, 2255–2270, 2016.

655 Ding, Y., Cheng, X., Liu, J., Hui, F., Wang, Z., and Chen, S.: Retrieval of Melt Pond Fraction  
656 over Arctic Sea Ice during 2000–2019 Using an Ensemble-Based Deep Neural Network.  
657 *Remote Sensing*. 12(17):2746. <https://doi.org/10.3390/rs12172746>, 2020

658 DuVivier, A. K., Holland, M. M., Landrum, L., Singh, H. A., Bailey, D. A., and Maroon, E.  
659 A.: Impacts of sea ice mushy thermodynamics in the Antarctic on the coupled Earth  
660 system. *Geophysical Research Letters*, 48, e2021GL094287.  
661 <https://doi.org/10.1029/2021GL094287>, 2021.

662 Fer, I.: Near-inertial mixing in the central Arctic Ocean. *J. Phys. Oceanogr.*, 44, 2031–2049,  
663 <https://doi.org/10.1175/JPO-D-13-0133.1>, 2014.

664 Fetterer, F., Knowles, K., Meier, W. N., Savoie, M., and Windnagel, A. K.: updated daily. Sea  
665 Ice Index, Version 3. Boulder, Colorado USA. NSIDC: National Snow and Ice Data  
666 Center. <https://doi.org/10.7265/N5K072F8>, 2017.

667 Freitas, S. R., Grell, G. A., Molod, A., Thompson, M. A., Putman, W. M., Santos e Silva, C.  
668 M. and Souza, E. P.: Assessing the Grell–Freitas convection parameterization in the

---

669 NASA GEOS modeling system. *J. Adv. Model. Earth Syst.*, 10, 1266–1289,  
670 <https://doi.org/10.1029/2017MS001251>, 2018.

671 Freitas, S. R., Grell, G. A., and Li, H.: The Grell–Freitas (GF) convection parameterization:  
672 recent developments, extensions, and applications, *Geosci. Model Dev.*, 14, 5393–5411,  
673 <https://doi.org/10.5194/gmd-14-5393-2021>, 2021.

674 Germe, A., Chevallier, M., y Méliá, D. S., Sanchez-Gomez, E., and Cassou, C.: Interannual  
675 predictability of Arctic sea ice in a global climate model: Regional contrasts and  
676 temporal evolution. *Climate Dynamics*, 43(9-10), 2519–2538, 2014.

677 Grell, G. A., and Freitas, S.: A scale and aerosol aware stochastic convective parameterization  
678 for weather and air quality modeling. *Atmos. Chem. Phys.*, 14, 5233–5250,  
679 <https://doi.org/10.5194/acp-14-5233-2014>, 2014.

680 Guemas, V., Blanchard-Wrigglesworth, E., Chevallier, M., Day, J. J., Déqué, M., Doblus-  
681 Reyes, F. J., et al.: A review on Arctic sea-ice predictability and prediction on seasonal  
682 to decadal time-scales. *Quarterly Journal of the Royal Meteorological Society*, 142(695),  
683 546–561, 2016.

684 Haidvogel, D. B., Arango, H., Budgell, W. P., Cornuelle, B. D., Curchitser, E., Di Lorenzo, E.,  
685 et al.: Ocean forecasting in terrain-following coordinates: Formulation and skill  
686 assessment of the Regional Ocean Modeling System, *Journal of Computational Physics*,  
687 227, 3595–3624, 2008.

688 Hecht, M. W., Wingate, B. A., and Kassis, P.: A better, more discriminating test problem for  
689 ocean tracer transport. *Ocean Modell.* 2 (1–2), 1–15. <https://doi.org/10.1016/S1463-50>  
690 [03\(00\)00004-4](https://doi.org/10.1016/S1463-5003(00)00004-4), 2000.

691 Hersbach, H., Bell, B., Berrisford, P., et al.: The ERA5 global reanalysis. *Quarterly Journal of*  
692 *the Royal Meteorological Society*, 146, 1999–2049. <https://doi.org/10.1002/qj.3803>,  
693 2020.

694 Horvat, C., and Tziperman, E.: A prognostic model of the sea-ice floe size and thickness  
695 distribution. *Cryosphere* 9, 2119–2134, 2015.

---

696 Horvat, C., Tziperman, E., and Campin, J.-M.: Interaction of sea ice floe size, ocean eddies,  
697 and sea ice melting. *Geophysical Research Letters*, 43, 8083–8090.  
698 <https://doi.org/10.1002/2016GL069742>, 2016.

699 Huang, Y., Chou, G., Xie, Y., & Soulard, N.: Radiative control of the interannual variability  
700 of Arctic sea ice. *Geophysical Research Letters*, 46, 9899– 9908.  
701 <https://doi.org/10.1029/2019GL084204>, 2019.

702 Itoh, M., Nishino, S., Kawaguchi, Y., and Kikuchi, T.: Barrow Canyon volume, heat, and  
703 freshwater fluxes revealed by long-term mooring observations between 2000 and 2008.  
704 *J. Geophys. Res. Oceans*, 118, 4363–4379, <https://doi.org/10.1002/jgrc.20290>, 2013.

705 Jung, T., Gordon, N.D., Bauer, P., Bromwich, D.H., Chevallier, M., Day, J.J., Dawson, J.,  
706 Doblas-Reyes, F., Fairall, C., Goessling, H.F., Holland, M., Inoue, J., Iversen, T., Klebe,  
707 S., Lemke, P., Losch, M., Makshtas, A., Mills, B., Nurmi, P., Perovich, D., Reid, P.,  
708 Renfrew, I.A., Smith, G., Svensson, G., Tolstykh, M., and Yang, Q.: Advancing Polar  
709 Prediction Capabilities on Daily to Seasonal Time Scales. *Bulletin of the American*  
710 *Meteorological Society*. <https://doi.org/10.1175/BAMS-D-14-00246.1>, 2016.

711 Kaleschke, L., Tian-Kunze, X., Maaß, N., Mäkynen, M., and Drusch, M.: Sea ice thickness  
712 retrieval from SMOS brightness temperatures during the Arctic freeze-up period.  
713 *Geophys. Res. Lett.*, L05501, <https://doi.org/10.1029/2012GL050916>, 2012.

714 Kapsch, M., Graversen, R. G., Tjernström, M., and Bintanja, R.: The Effect of Downwelling  
715 Longwave and Shortwave Radiation on Arctic Summer Sea Ice. *Journal of Climate* 29,  
716 3, 1143-1159, <https://doi.org/10.1175/JCLI-D-15-0238.1>, 2016.

717 Kay, J. E., L’Ecuyer, T., Gettelman, A., Stephens, G., and O’Dell, C.: The contribution of cloud  
718 and radiation anomalies to the 2007 Arctic sea ice extent minimum, *Geophys. Res. Lett.*,  
719 35, L08503, doi:10.1029/2008GL033451, 2008.

720 Keen, A., Blockley, E., Bailey, D. A., Boldingh Debernard, J., Bushuk, M., Delhaye, S.,  
721 Docquier, D., Feltham, D., Massonnet, F., O’Farrell, S., Ponsoni, L., Rodriguez, J. M.,  
722 Schroeder, D., Swart, N., Toyoda, T., Tsujino, H., Vancoppenolle, M., and Wyser, K.:

---

723 An inter-comparison of the mass budget of the Arctic sea ice in CMIP6 models, *The*  
724 *Cryosphere*, 15, 951–982, <https://doi.org/10.5194/tc-15-951-2021>, 2021.

725 Kirkman, C. H., IV, and Bitz, C. M.: The Effect of the Sea Ice Freshwater Flux on Southern  
726 Ocean Temperatures in CCSM3: Deep-Ocean Warming and Delayed Surface Warming.  
727 *Journal of Climate* 24, 9, 2224–2237, <https://doi.org/10.1175/2010JCLI3625.1>, 2011.

728 Kwok, R.: Arctic sea ice thickness, volume, and multiyear ice coverage: Losses and coupled  
729 variability (1958–2018). *Environmental Research Letters*, 13(10), 105005, 2018

730 Laxon, S., Giles, K. A., Ridout, A. L., Wingham, D. J., Willatt, R., Cullen, R., Kwok, R.,  
731 Schweiger, A., Zhang, J., Haas, C., Hendricks, S., Krishfield, R., Kurtz, N., Farrell, S.,  
732 and Davidson, M.: CryoSat-2 estimates of Arctic sea ice thickness and volume, *Geophys.*  
733 *Res. Lett.*, 40, <https://doi.org/10.1002/grl.50193>, 2013.

734 Lemieux, J. F., Dupont, F., Blain, P., Roy, F., Smith, G. C., and Flato, G. M.: Improving the  
735 simulation of landfast ice by combining tensile strength and a parameterization for  
736 grounded ridges. *J. Geophys. Res. Oceans*, 121:7354–7368,  
737 <http://dx.doi.org/10.1002/2016JC012006>, 2016.

738 Leonard, B., Mokhtari, S.: ULTRA-SHARP Non oscillatory Convection Schemes for High-  
739 Speed Steady Multidimensional Flow. Technical Report. NASA, 1990.

740 Liang, X., and Losch, M.: On the effects of increased vertical mixing on the Arctic Ocean and  
741 sea ice. *Journal of Geophysical Research: Oceans*, 123, 9266– 9282.  
742 <https://doi.org/10.1029/2018JC014303>, 2018.

743 Liu, J., Song, M., Horton, R., and Hu, Y.: Revisiting the potential of melt pond fraction as a  
744 predictor for the seasonal Arctic sea ice minimum. *Environmental Research Letters*, 10,  
745 054017. <https://doi.org/10.1088/1748-9326/10/5/054017>, 2015.

746 Liu, J., Chen, Z., Hu, Y., Zhang, Y., Ding, Y., Cheng, X., et al.: Towards reliable arctic sea ice  
747 prediction using multivariate data assimilation. *Science Bulletin*, 64(1), 63–72, 2019.

---

748 Merryfield, W., Lee, W.-S., Wang, W., Chen, M., and Kumar, A.: Multi-system seasonal  
749 predictions of Arctic sea ice. *Geophysical Research Letters*, 40, 1551–1556.  
750 <https://doi.org/10.1002/grl.50317>, 2013.

751 Mallett, R. D. C., Stroeve, J. C., Cornish, S. B. Crawford, A. D., Lukovich, J. V., Serreze, M.  
752 C., Barrett, A. P., Meier, W. N., Heorton, H. D. B. S., and Tsamados, M.: Record winter  
753 winds in 2020/21 drove exceptional Arctic sea ice transport. *Commun Earth Environ* 2,  
754 149, <https://doi.org/10.1038/s43247-021-00221-8>, 2021.

755 Maslanik, J. and Stroeve, J.: Near-Real-Time DMSP SSMIS Daily Polar Gridded Sea Ice  
756 Concentrations, Version 1. Boulder, Colorado USA. NASA National Snow and Ice Data  
757 Center Distributed Active Archive Center. <https://doi.org/10.5067/U8C09DWVX9LM>,  
758 1999.

759 McLaughlin, F. A., Carmack, E. C., Williams, W. J., Zimmerman, S., Shimada, K., and Itoh,  
760 M.: Joint effects of boundary currents and thermohaline intrusions on the warming of  
761 Atlantic water in the Canada Basin, 1993–2007. *J. Geophys. Res.*, 114, C00A12,  
762 <https://doi.org/10.1029/2008JC005001>, 2009.

763 Meehl, G.A., Stocker, T. F., Collins, W. D., et al.: Global Climate Projections. In: *Climate*  
764 *Change 2007: The Physical Science Basis. Contribution of Working Group I to the*  
765 *Fourth Assessment Report of the Intergovernmental Panel on Climate Change* [Solomon,  
766 S., D. Qin, M. Manning, Z. Chen, M. Marquis, K.B. Averyt, M. Tignor and H.L. Miller  
767 (eds.)]. Cambridge University Press, Cambridge, United Kingdom and New York, NY,  
768 USA, 2007.

769 Msadek, R., Vecchi, G., Winton, M., and Gudgel, R.: Importance of initial conditions in  
770 seasonal predictions of Arctic sea ice extent. *Geophysical Research Letters*, 41, 5208–  
771 5215. <https://doi.org/10.1002/2014GL060799>, 2014.

772 Nakanishi, M., and Niino., H.: Development of an improved turbulence closure model for the  
773 atmospheric boundary layer. *J. Meteor. Soc. Japan*, 87, 895–912,  
774 <https://doi.org/10.2151/jmsj.87.895>, 2009.

---

775 Naughten, K. A., Galton-Fenzi, B. K., Meissner, K. J., England, M. H., Brassington, G. B.,  
776 Colberg, F., Hattermann, T., and Debernard, J. B.: Spurious sea ice formation caused by  
777 oscillatory ocean tracer advection schemes. *Ocean Model.*, 116, 108–117, 2017.

778 Naughten, K. A., Meissner, K. J., Galton-Fenzi, B. K., England, M. H., Timmermann, R.,  
779 Hellmer, H. H., Hattermann, T., and Debernard, J. B.: Intercomparison of Antarctic ice-  
780 shelf, ocean, and sea-ice interactions simulated by MetROMS-iceshelf and FESOM 1.4.  
781 *Geosci. Model. Dev.*, 11, 1257–1292, 2018

782 Nerger, L., and Hiller, W.: Software for Ensemble-based Data Assimilation Systems -  
783 Implementation Strategies and Scalability. *Computers and Geosciences*, 55, 110-118.  
784 <https://doi.org/10.1016/j.cageo.2012.03.026>, 2013.

785 Nerger, L., Janjić, T., Schröter, J. and Hiller, W.: A unification of ensemble square root Kalman  
786 filters. *Monthly Weather Review*, 140, 2335-2345. [https://doi.org/10.1175/MWR-D-11-](https://doi.org/10.1175/MWR-D-11-00102.1)  
787 [00102.1](https://doi.org/10.1175/MWR-D-11-00102.1), 2012.

788 Newton, R., Pfirman, S., Schlosser, P., Tremblay, B., Murray, M. and Pomerance, R.: White  
789 Arctic vs. Blue Arctic: A case study of diverging stakeholder responses to environmental  
790 change. *Earth's Future*, 4: 396-405. <https://doi.org/10.1002/2016EF000356>, 2016.

791 Nicolaus M., Katlein, C., Maslanik, J., and Hendricks, S.: Changes in Arctic sea ice result in  
792 increasing light transmittance and absorption. *Geophysical Research Letters*, 39, L24501.  
793 <https://doi.org/10.1029/2012GL053738>, 2012

794 Nicolaus M., and Katlein, C.: Mapping radiation transfer through sea ice using a remotely  
795 operated vehicle (ROV). *The Cryosphere*, 7, 763-77. [https://doi.org/10.5194/tc-7-763-](https://doi.org/10.5194/tc-7-763-2013)  
796 [2013](https://doi.org/10.5194/tc-7-763-2013), 2013.

797 Notz, D., Jahn, A., Holland, M., Hunke, E., Massonnet, F., Stroeve, J., Tremblay, B., and  
798 Vancoppenolle, M.: The CMIP6 Sea-Ice Model Intercomparison Project (SIMIP):  
799 understanding sea ice through climate-model simulations, *Geosci. Model Dev.*, 9, 3427–  
800 3446, <https://doi.org/10.5194/gmd-9-3427-2016>, 2016.

---

801 Ogi, M., Yamazaki, K., and Wallace, J. M.: Influence of winter and summer surface wind  
802 anomalies on summer Arctic sea ice extent, *Geophys. Res. Lett.*, 37, L07701,  
803 doi:10.1029/2009GL042356, 2010.

804 Olonscheck, D., Mauritsen, T. and Notz, D.: Arctic sea-ice variability is primarily driven by  
805 atmospheric temperature fluctuations. *Nat. Geosci.* 12, 430–434,  
806 <https://doi.org/10.1038/s41561-019-0363-1>, 2019.

807 Padman, L., and Dillon, T. M.: Vertical heat fluxes through the Beaufort Sea thermohaline  
808 staircase. *J. Geophys. Res.*, 92, 10 799–10 806,  
809 <https://doi.org/10.1029/JC092iC10p10799>, 1987.

810 Perovich, D., Richter-Menge, J., Jones, K., Light, B., Elder, B., Polashenski, C., Laroche, D.,  
811 Markus, T., and Lindsay, R.: Arctic sea-ice melt in 2008 and the role of solar heating.  
812 *Annals of Glaciology*, 52(57), 355-359. doi:10.3189/172756411795931714, 2011.

813 Perovich, D., Richter-Menge, J., Polashenski, C., Elder, B., Arbetter, T., and Brennick, O.: Sea  
814 ice mass balance observations from the North Pole Environmental Observatory,  
815 *Geophys. Res. Lett.*, 41, 2019– 2025, doi:10.1002/2014GL059356, 2014.

816 Peterson, K., Arribas, A., Hewitt, H., Keen, A., Lea, D., and McLaren, A.: Assessing the  
817 forecast skill of Arctic sea ice extent in the GloSea4 seasonal prediction system. *Climate*  
818 *Dynamics*, 44(1-2), 147–162, 2015.

819 Pham, D. T.: Stochastic methods for sequential data assimilation in strongly nonlinear systems.  
820 *Mon. Wea. Rev.*, 129, 1194–1207, 2001.

821 Rasch, P. J.: Conservative shape-preserving two-dimensional transport on a spherical reduced  
822 grid, *Mon. Wea. Rev.*, 122, 1337-1350, 1994.

823 Reynolds, R. W., Smith, T. M., Liu, C., Chelton, D. B., Casey, K. S., and Schlax, M. G.: Daily  
824 High-Resolution-Blended Analyses for Sea Surface Temperature, *Journal of Climate*,  
825 20(22), 5473-5496, 2007.

---

826 Ricker, R., Hendricks, S., Kaleschke, L., Tian-Kunze, X., King, J., and Haas, C.: A weekly  
827 Arctic sea-ice thickness data record from merged CryoSat-2 and SMOS satellite data,  
828 *The Cryosphere*, 11, 1607–1623, <https://doi.org/10.5194/tc-11-1607-2017>, 2017.

829 Roach, L. A., Bitz, C. M., Horvat, C., and Dean, S. M.: Advances in modeling interactions  
830 between sea ice and ocean surface waves. *Journal of Advances in Modeling Earth*  
831 *Systems*, 11. <https://doi.org/10.1029/2019MS001836>, 2019.

832 Roach, L. A., Horvat, C., Dean, S. M., and Bitz, C. M.: An emergent sea ice floe size  
833 distribution in a global coupled ocean–sea ice model. *Journal of Geophysical Research:*  
834 *Oceans*, 123(6), 4322–4337. <https://doi.org/10.1029/2017JC013692>, 2018.

835 Rocheta, E., Evans, J. P., and Sharma, A.: Can Bias Correction of Regional Climate Model  
836 Lateral Boundary Conditions Improve Low-Frequency Rainfall Variability?, *Journal of*  
837 *Climate*, 30(24), 9785–9806, 2017.

838 Rocheta, E., Evans, J. P. and Sharma, A.: Correcting lateral boundary biases in regional climate  
839 modelling: the effect of the relaxation zone. *Clim. Dyn.*, 55, 2511–2521.  
840 <https://doi.org/10.1007/s00382-020-05393-1>, 2020.

841 Serreze, M. C. and Meier, W. N.: The Arctic's sea ice cover: trends, variability, predictability,  
842 and comparisons to the Antarctic. *Ann. N.Y. Acad. Sci.*, 1436: 36–53.  
843 <https://doi.org/10.1111/nyas.13856>, 2019.

844 Saha, S., Moorthi, S., Wu, X., et al.: The NCEP climate forecast system version 2. *J. Clim.*  
845 27:2185–2208, 2014.

846 Schmidt, G. A., Bitz, C. M., Mikolajewicz, U., and Tremblay, L.-B.: Ice–ocean boundary  
847 conditions for coupled models, *Ocean Model.*, 7, 59–74, 2004.

848 Shchepetkin, A.F., McWilliams, J. C.: Quasi-monotone advection schemes based on explicit  
849 locally adaptive dissipation. *Mon. Weather Rev.* 126 (6), 1541–1580, 1998.

850 Shchepetkin, A. F., and McWilliams, J. C.: The Regional Ocean Modeling System: A split-  
851 explicit, free-surface, topography following coordinates ocean model, *Ocean Modelling*,  
852 9, 347–404, 2005.



---

853 Shi, X., Notz, D., Liu, J., Yang, H., and Lohmann, G.: Sensitivity of Northern Hemisphere  
854 climate to ice–ocean interface heat flux parameterizations, *Geosci. Model Dev.*, 14,  
855 4891–4908, <https://doi.org/10.5194/gmd-14-4891-2021>, 2021.

856 Sigmond, M., Fyfe, J., Flato, G., Kharin, V., and Merryfield, W.: Seasonal forecast skill of  
857 Arctic sea ice area in a dynamical forecast system. *Geophysical Research Letters*, 40,  
858 529–534. <https://doi.org/10.1002/grl.50129>, 2013.

859 Skamarock, W. C., Klemp, J. B., Dudhia, J., Gill, D. O., Barker, D. M., Wang, W. and Powers,  
860 J. G.: A Description of the Advanced Research WRF Version 2. NCAR Technical Note,  
861 NCAR/TN-468+STR, 2005.

862 Smolarkiewicz, P. K.: Multidimensional positive definite advection transport algorithm: An  
863 overview. *Int. J. Numer. Methods Fluids*, 50, 1123–1144, 2006.

864 Song, Y. and Haidvogel, D. B.: A semi-implicit ocean circulation model using a generalized  
865 topography-following coordinate system. *J. Comp. Phys.*, 115(1), 228-244, 1994.

866 Steele, M.: Sea ice melting and floe geometry in a simple ice-ocean model. *Journal of*  
867 *Geophysical Research: Oceans*, 97(C11), 17,729–17,738.  
868 <https://doi.org/10.1029/92JC01755>, 1992.

869 Stroeve, J., Blanchard-Wrigglesworth, E., Guemas, V., Howell, S., Massonnet, F., and Tietsche,  
870 S.: Improving predictions of Arctic sea ice extent, *Eos*, 96,  
871 <https://doi.org/10.1029/2015EO031431>, 2015.

872 Stroeve, J., Hamilton, L. C., Bitz, C. M., and Blanchard-Wrigglesworth, E.: Predicting  
873 September sea ice: Ensemble skill of the SEARCH Sea Ice Outlook 2008 – 2013,  
874 *Geophys. Res. Lett.*, 41, 2411-2418, <https://doi.org/10.1002/2014GL059388>, 2014.

875 Tian-Kunze, X., Kaleschke, L., Maaß, N., Mäkynen, M., Serra, N., Drusch, M., and Krumpen,  
876 T.: SMOS-derived thin sea ice thickness: Algorithm baseline, product specifications and  
877 initial verification. *Cryosphere*, 8, 997-1018, <https://doi.org/10.5194/tc-8-997-2014>,  
878 2014.

---

879 Tietsche, S., Day, J., Guemas, V., Hurlin, W., Keeley, S., Matei, D., et al.: Seasonal to  
880 interannual Arctic sea ice predictability in current global climate models. *Geophysical*  
881 *Research Letters*, 41, 1035–1043. <https://doi.org/10.1002/2013GL058755>, 2014.

882 Tsamados, M., Feltham, D. L., and Wilchinsky, A. V.: Impact of a new anisotropic rheology  
883 on simulations of Arctic sea ice, *J. Geophys. Res. Oceans*, 118, 91–107,  
884 doi:10.1029/2012JC007990, 2013.

885 Turner, A. K., and Hunke, E. C.: Impacts of a mushy-layer thermodynamic approach in global  
886 sea-ice simulations using the CICE sea-ice model, *J. Geophys. Res. Oceans*, 120, 1253-  
887 1275, doi:10.1002/2014JC010358, 2015.

888 Turner, A. K., Hunke, E. C., and Bitz, C. M.: Two modes of sea-ice gravity drainage: A  
889 parameterization for large-scale modeling, *J. Geophys. Res.*, 118, 2279–2294,  
890 doi:10.1002/jgrc.20171, 2013.

891 Turner, J. S.: *Buoyancy Effects in Fluids*. Cambridge University Press, 368 pp. 1973.

892 Van den Dool, H.: *Empirical Methods in Short-Term Climate Prediction*, Oxford Univ. Press,  
893 Oxford, U. K., 2006.

894 Wang, W., Chen, M., and Kumar, A.: Seasonal prediction of Arctic sea ice extent from a  
895 coupled dynamical forecast system. *Monthly Weather Review*, 141(4), 1375–1394, 2013.

896 Warner, J. C., Armstrong, B., He, R., and Zambon, J.: Development of a coupled ocean–  
897 atmosphere–wave–sediment transport (COAWST) modeling system. *Ocean Modell.* 35,  
898 230–244, 2010.

899 Woodgate, R. A., Aagaard, K., and Weingartner, T. J.: A year in the physical oceanography of  
900 the Chukchi Sea: Moored measurements from autumn 1990–1991. *Deep-Sea Res. II*, 52,  
901 3116–3149, <https://doi.org/10.1016/j.dsr2.2005.10.016>, 2005.

902 Wu, W., Lynch, A. H., and Rivers, A.: Estimating the Uncertainty in a Regional Climate Model  
903 Related to Initial and Lateral Boundary Conditions, *Journal of Climate*, 18(7), 917-933,  
904 2005.

---

905 Yang, C.-Y., Liu, J., and Xu, S.: Seasonal Arctic sea ice prediction using a newly developed  
906 fully coupled regional model with the assimilation of satellite sea ice observations.  
907 Journal of Advances in Modeling Earth Systems, 12, e2019MS001938.  
908 <https://doi.org/10.1029/2019MS001938>, 2020.

909 Zampieri, L., Goessling, H. F., and Jung, T.: Bright prospects for Arctic sea ice prediction on  
910 subseasonal time scales. Geophysical Research Letters, 45, 9731– 9738.  
911 <https://doi.org/10.1029/2018GL079394>, 2018.

912 Zhang, J. and Rothrock, D.: Modeling global sea ice with a thickness and enthalpy distribution  
913 model in generalized curvilinear coordinates. Mon. Wea. Rev., 131, 845–861, 2003.

914 Zhang, J., Lindsay, R., Steele, M., and Schweiger, A.: What drove the dramatic retreat of arctic  
915 sea ice during summer 2007?, Geophys. Res. Lett., 35, L11505,  
916 [doi:10.1029/2008GL034005](https://doi.org/10.1029/2008GL034005), 2008.

917 Zhang, J., Schweiger, A., Steele, M., and Stern, H.: Sea ice floe size distribution in the marginal  
918 ice zone: Theory and numerical experiments. Journal of Geophysical Research: Oceans,  
919 120, 3484–3498. <https://doi.org/10.1002/2015JC010770>, 2015.

920 Zhang, J., Stern, H., Hwang, B., Schweiger, A., Steele, M., Stark, M., and Graber, H. C.:  
921 Modeling the seasonal evolution of the Arctic sea ice floe size distribution. Elementa:  
922 Science of the Anthropocene, 4(1), 126.  
923 <https://doi.org/10.12952/journal.elementa.000126>, 2016.  
924

925 **7. Tables**

926 Table 1 The summary of physic parameterizations used in the Y21\_CRTL experiment

WRF physics	
Cumulus parameterization	Grell-Freitas (Freitas et al. 2018; improved from Y20)
Microphysics parameterization	Morrison 2-moment (Morrison et al. 2009; same as Y20)
Longwave radiation parameterization	CAM spectral band scheme (Collins et al. 2004; same as Y20)
Shortwave radiation parameterization	CAM spectral band scheme (Collins et al. 2004; same as Y20)
Boundary layer physics	MYNN2 (Nakanishi and Niino, 2006; improved from Y20)
Land surface physics	Unified Noah LSM (Chen and Dudhia, 2001; improved from Y20)
ROMS physics	
Tracer advection scheme	MPDATA (Smolarkiewicz, 2006; same as Y20)
Tracer vertical mixing scheme	GLS (Umlauf and Burchard, 2003; same as Y20)

Bottom drag scheme	Quadratic bottom friction (QDRAG; (same as Y20)
CICE physics	
Ice dynamics	EVP (Hunke and Dukowicz, 1997; improved from Y20)
Ice thermodynamics	Bitz and Lipscomb (1999; same as Y20)
Shortwave albedo	Delta-Eddington (Briegleb and Light, 2007; same as Y20)

927

928

929 Table 2 The summary of the prediction experiments and details of experiment designs.

930 Note: All experiments use the CFS operational forecasts as initial and boundary conditions; VT:

931 vertical transformation function; VS: vertical stretching function; SH94: stretching function of

932 Song and Haidvogel (1994); S10: stretching function of Shchepetkin (2010).

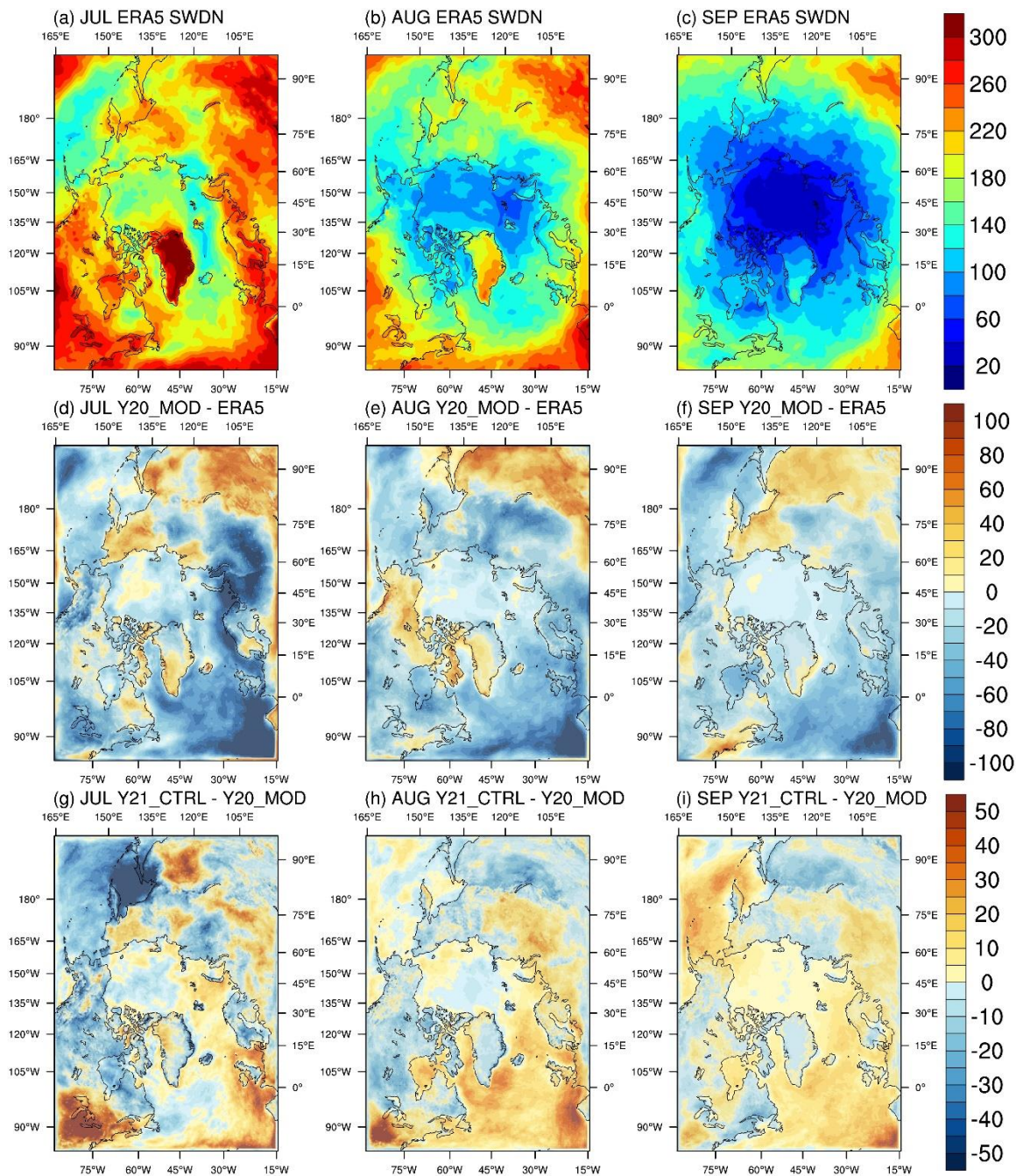
Experiment	Physics	Assimilation	ROMS vertical coordinate	Simulation period
Y20_MOD	Physics (old version)  listed in Table 1	6 localization radii  SSMIS SIC  Simply-merged CryoSat- 2/SMOS SIT	VT 1  VS SH94  $h_c$ 10m	2018.07.01-  2018.10.01
Y21_CTRL	Physics (new version)  listed in Table 1	6 localization radii  SSMIS SIC  Simply-merged CryoSat- 2/SMOS SIT	VT 1  VS SH94  $h_c$ 10m	2018.07.01-  2018.10.01
Y21_VT	Physics (new version)  listed in Table 1	6 localization radii  SSMIS SIC  Simply-merged CryoSat- 2/SMOS SIT	VT 2  VS S10  $h_c$ 300m	2018.07.01-  2018.10.01
Y21_RP	Advection: U3H/C4V	6 localization radii	VT 2	2018.07.01-

		SSMIS SIC Simply-merged CryoSat- 2/SMOS SIT	VS S10 $h_c$ 300m	2018.10.01
Y21_MUSHY	Same physics as Y21_RP CICE: Mushy layer thermodynamics	6 localization radii SSMIS SIC Simply-merged CryoSat- 2/SMOS SIT	VT 2 VS S10 $h_c$ 300m	2018.07.01- 2018.10.01
Y21_SIT	Same physics as Y21_RP	6 localization radii SSMIS SIC OI-merged CryoSat- 2/SMOS SIT	VT 2 VS S10 $h_c$ 300m	2018.07.01- 2018.10.01
Y21_EXT-7	Same physics as Y21_RP	6 localization radii SSMIS SIC OI-merged CryoSat- 2/SMOS SIT	VT 2 VS S10 $h_c$ 300m	2018.07.01- 2019.01.31

933

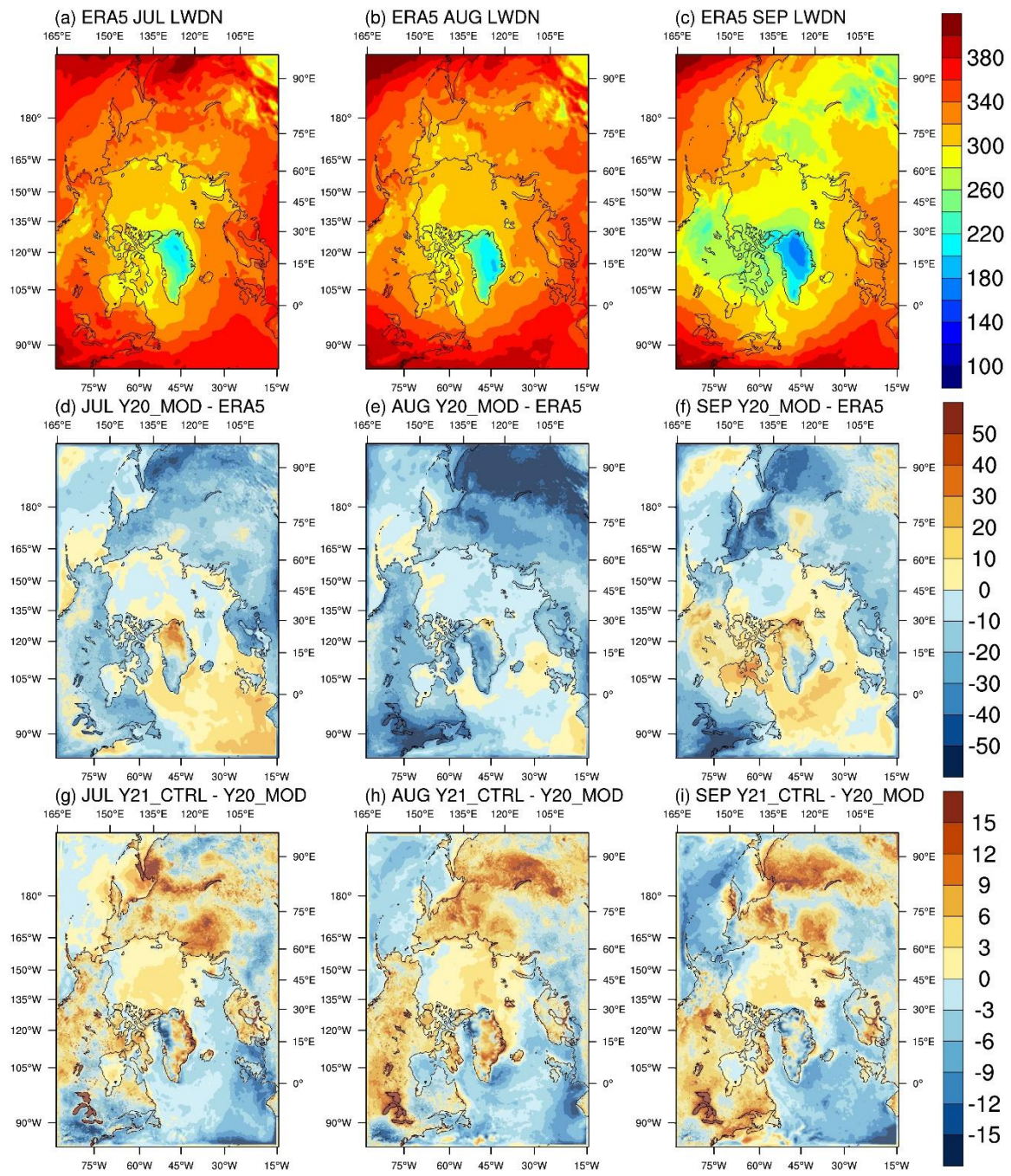
934

935 **8. Figures**



936  
 937 Figure 1 ERA5 monthly mean of downward shortwave radiation at the surface for (a) July, (b)  
 938 August, and (c) September, the difference between Y20\_MOD and ERA5 for (d) July, (e)  
 939 August, (f) September, and the difference between Y21\_CTRL (changes in the atmospheric  
 940 physics) and Y20\_MOD (the original CAPS) for (g) July, (h) August, and (i) September.  
 941

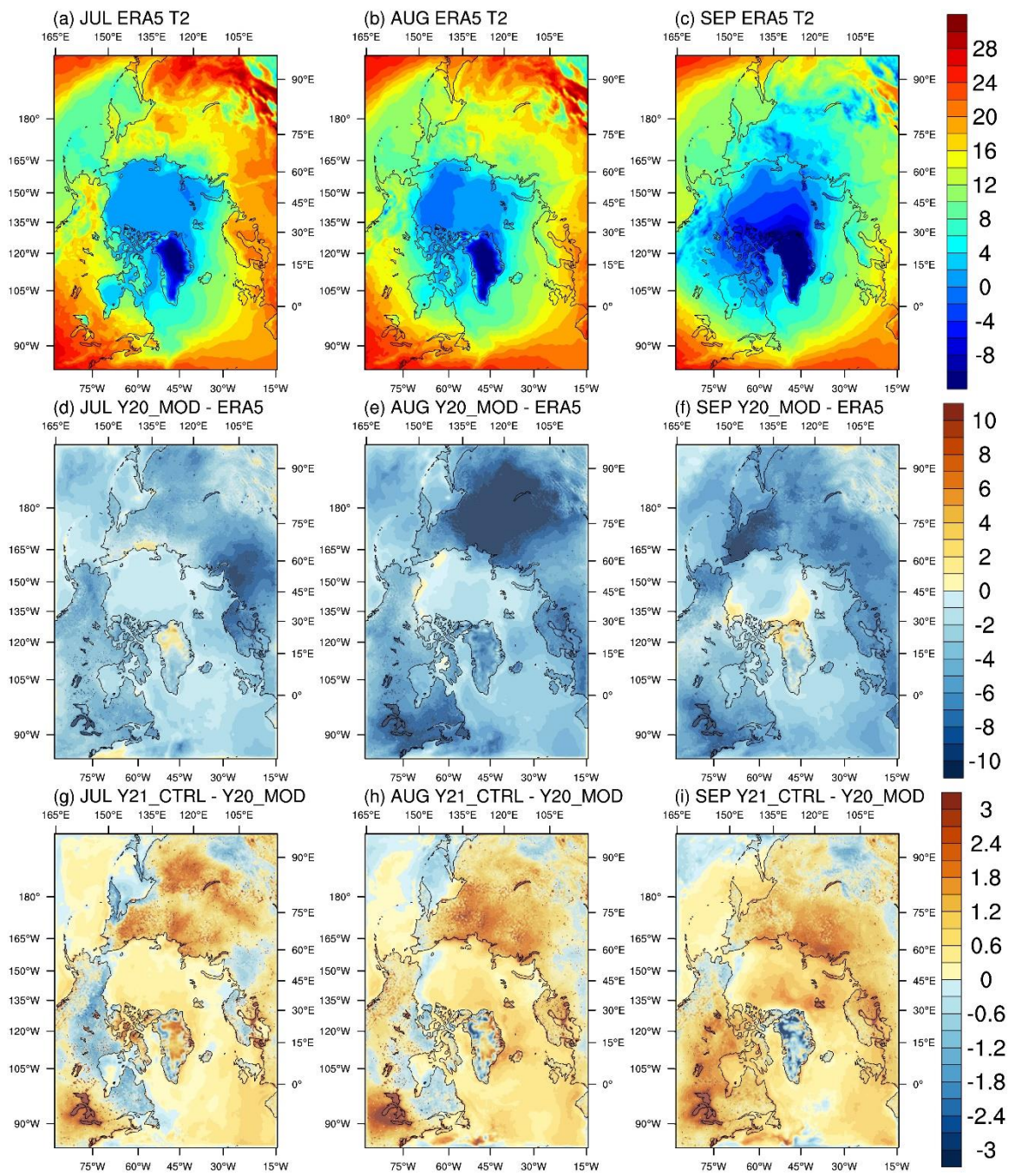




942

943 Figure 2 Same as Figure 1, but for downward thermal radiation at the surface.

944



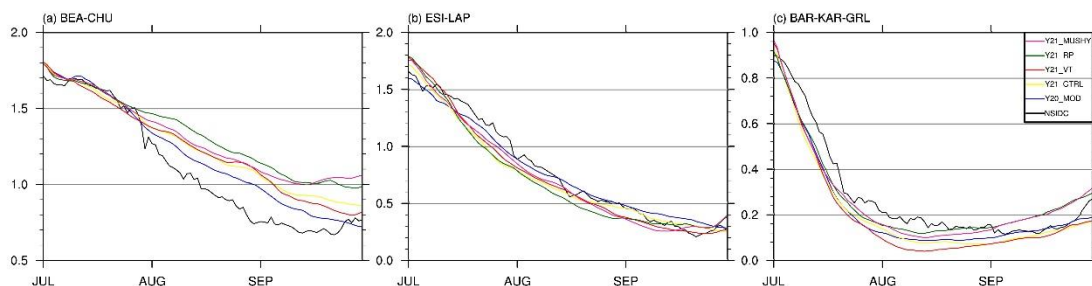
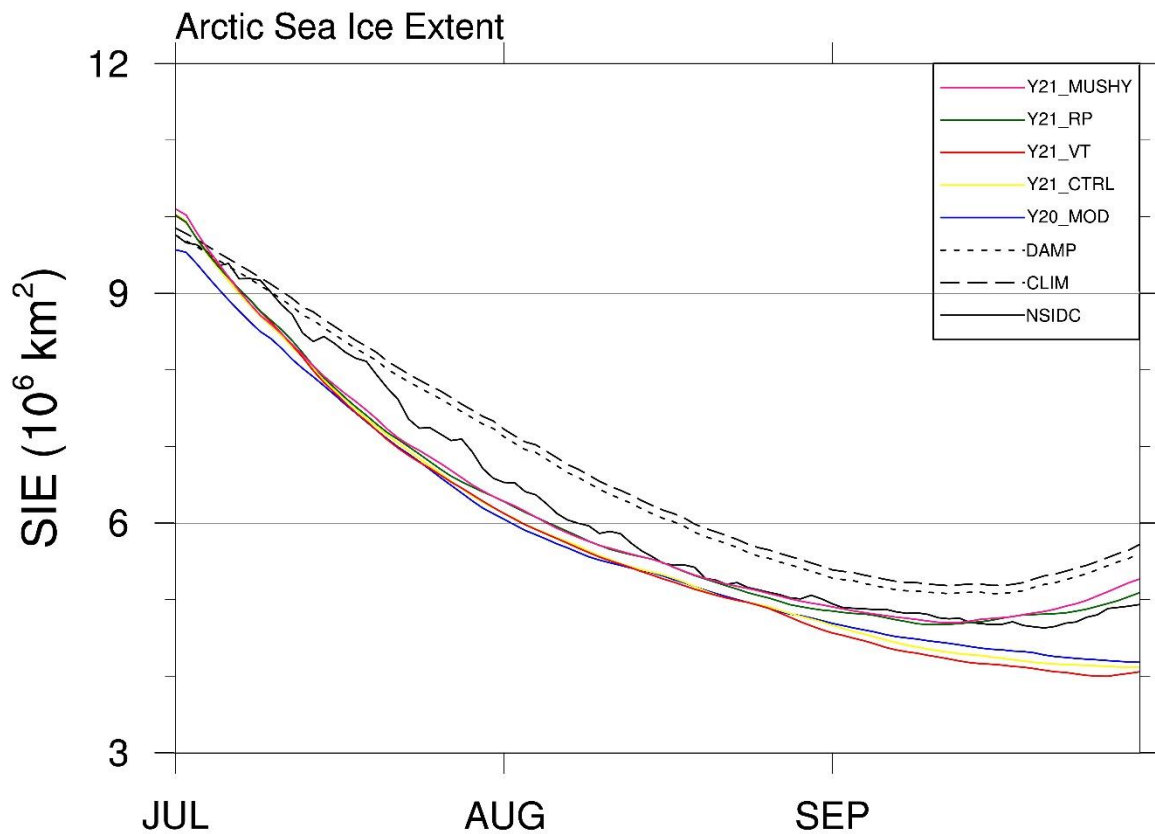
945

946 Figure 3 Same as Figure 1, but for near-surface air temperature.

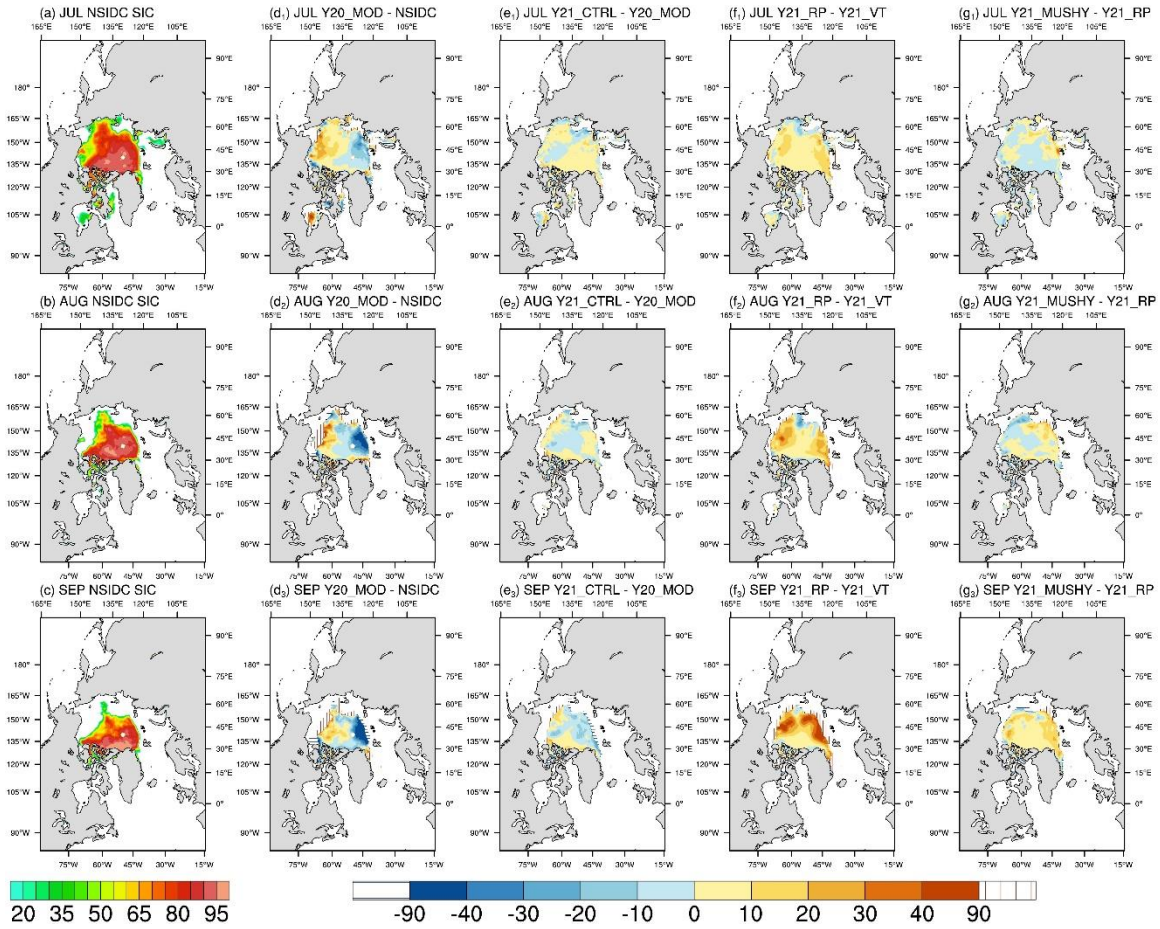
947

948





949  
 950 Figure 4 Top panel: Time-series of Arctic sea ice extent for the observations (black line) and  
 951 the ensemble-mean of Y20\_MOD (blue line, the original CAPS), Y21\_CTRL (yellow line,  
 952 changes in the atmospheric physics), Y21\_VT (red line, changes in the ocean vertical  
 953 coordinate), Y21\_RP (green line, changes in the oceanic advection), and Y21\_MUSHY (pink  
 954 line, changes in sea ice thermodynamics). Dashed and dotted lines are the climatology and the  
 955 damped anomaly persistence predictions. Bottom panel: Time-series of the observed (black  
 956 line) and the ensemble-mean of regional sea ice extents for Y20\_MOD (blue line), Y21\_CTRL  
 957 (yellow line), Y21\_VT (red line), Y21\_RP (green line), and Y21\_MUSHY (pink line) for (a)  
 958 Beaufort-Chukchi Seas, (b) East Siberian-Laptev Seas, and (c) Barents-Kara-Greenland Seas.

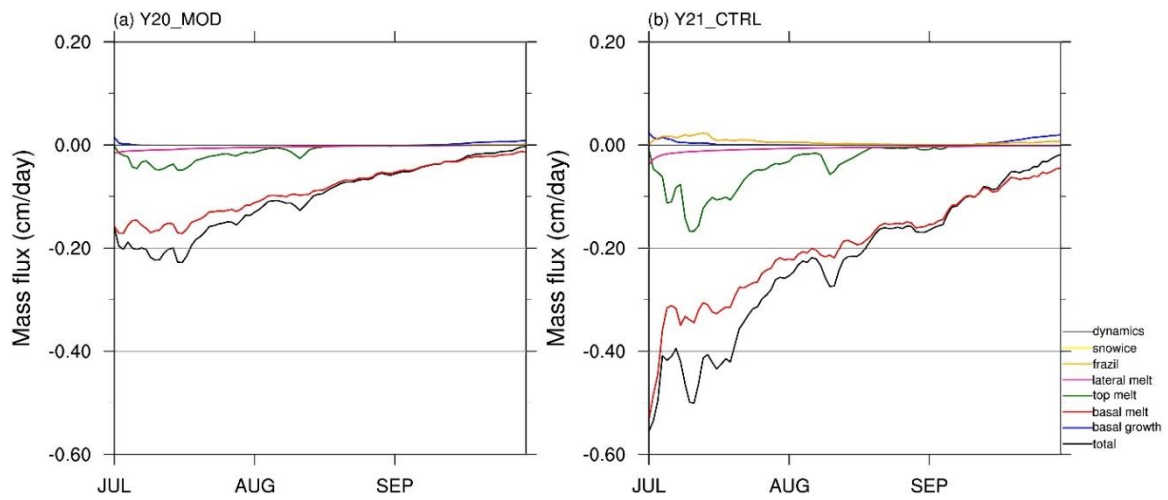


959

960 Figure 5 Monthly mean of sea ice concentration for (a) July, (b) August, (c) September of the  
 961 NSIDC observations, and the difference between the all prediction experiments and the  
 962 observations for (d<sub>1</sub>-g<sub>1</sub>) July, (d<sub>2</sub>-g<sub>2</sub>) August, (d<sub>3</sub>-g<sub>3</sub>) September. Vertical/horizontal-line areas  
 963 represent the difference of ice edge location (15% concentration).

964

965



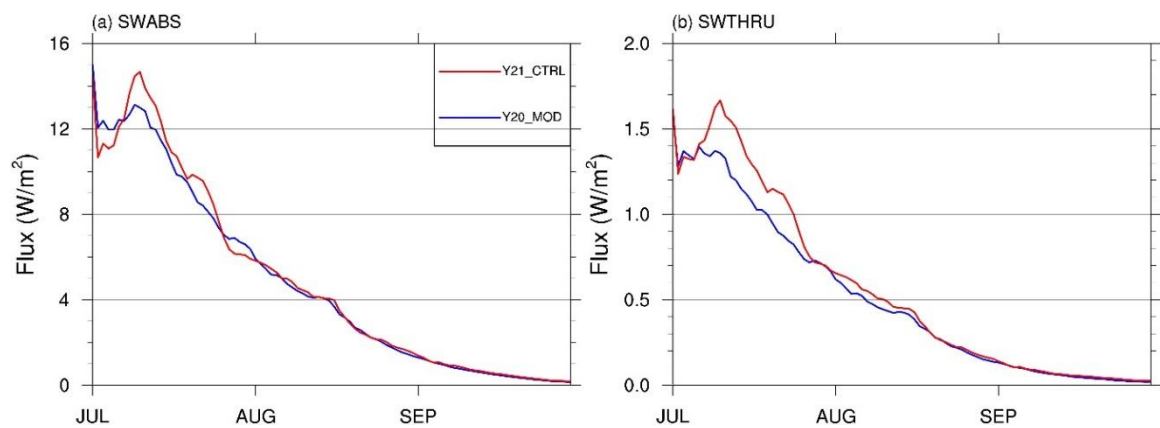
966

967 Figure 6 Time-series of sea ice mass budget terms for (a) Y20\_MOD (the original CAPS) and

968 (b) Y21\_CTRL (changes in the atmospheric physics).

969

970



971

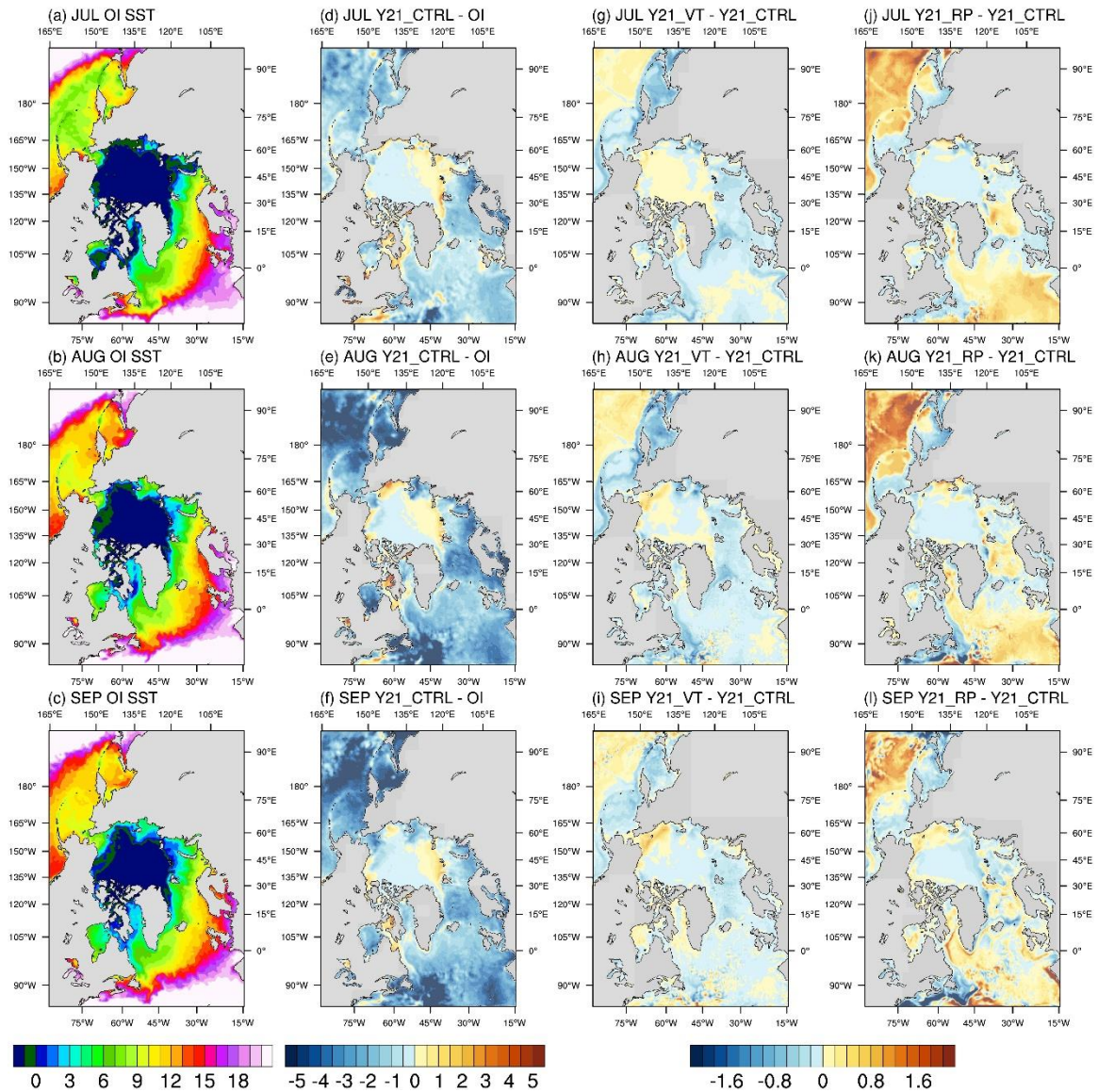
972

973

974

975

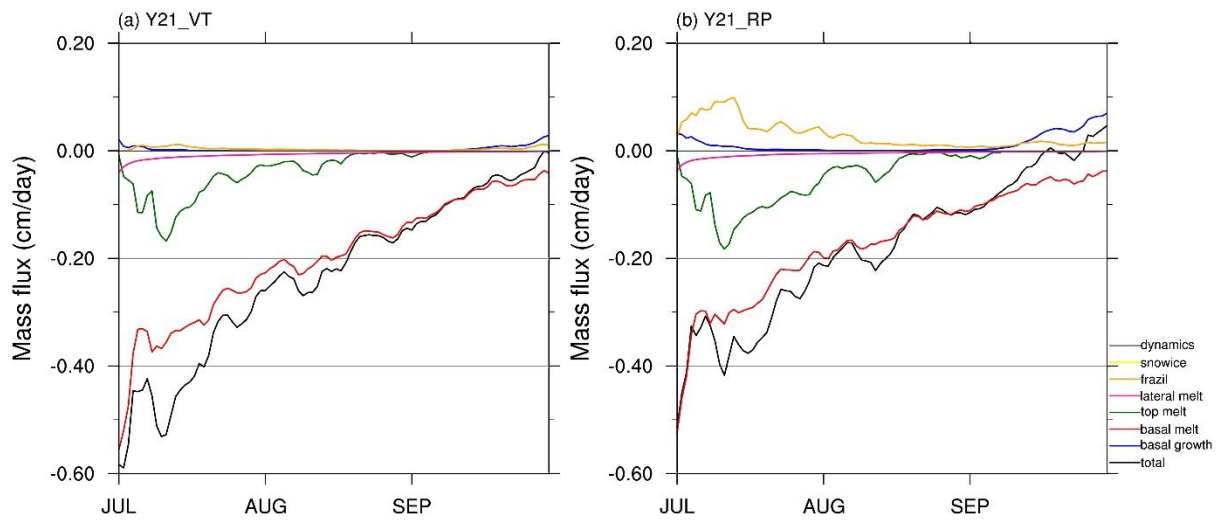
Figure 7 Time-series of (a) shortwave radiation absorbed by ice surface, and (b) penetrating shortwave radiation to the upper ocean averaged over ice-covered grid cells for Y20\_MOD (blue line, the original CAPS) and Y21\_CTRL (red line, changes in the atmospheric physics).



976

977 Figure 8 First column: monthly mean of sea surface temperature for (a) July, (b) August, (c)  
 978 September of the OI SST. Second column: the difference between Y21\_CTRL and the OI SST  
 979 for (d) July, (e) August, (f) September. Right panel: Monthly mean of sea surface temperature  
 980 difference between Y21\_VT/Y21\_RP and Y21\_CTRL for (g) July, (h) August, (i) September  
 981 of Y21\_VT, (j) July, (k) August, and (l) September of Y21\_RP.

982



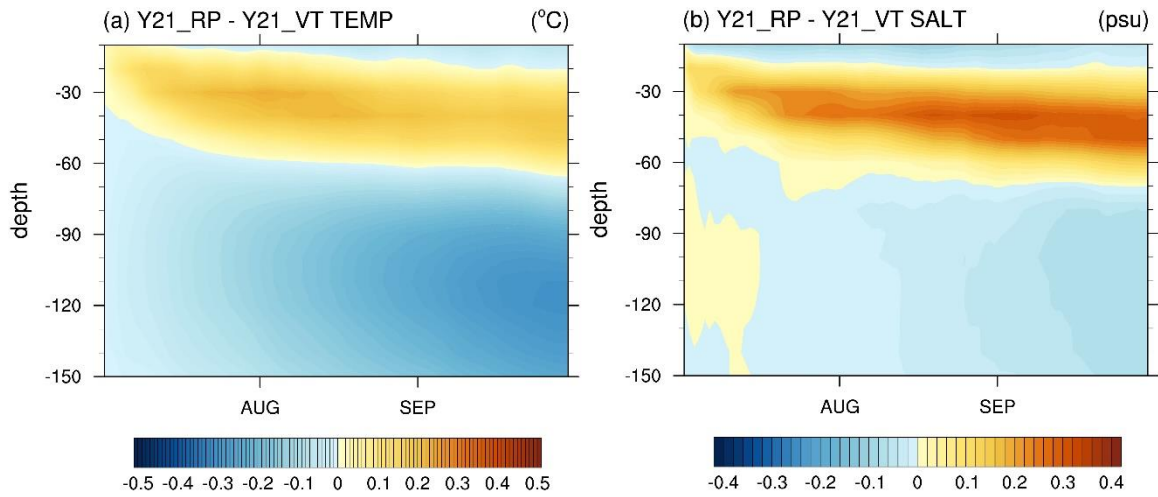
983

984 Figure 9 Same as Figure 6, but for (a) Y21\_VT (changes in the ocean vertical coordinate), and

985 (b) Y21\_RP (changes in the oceanic advection).

986

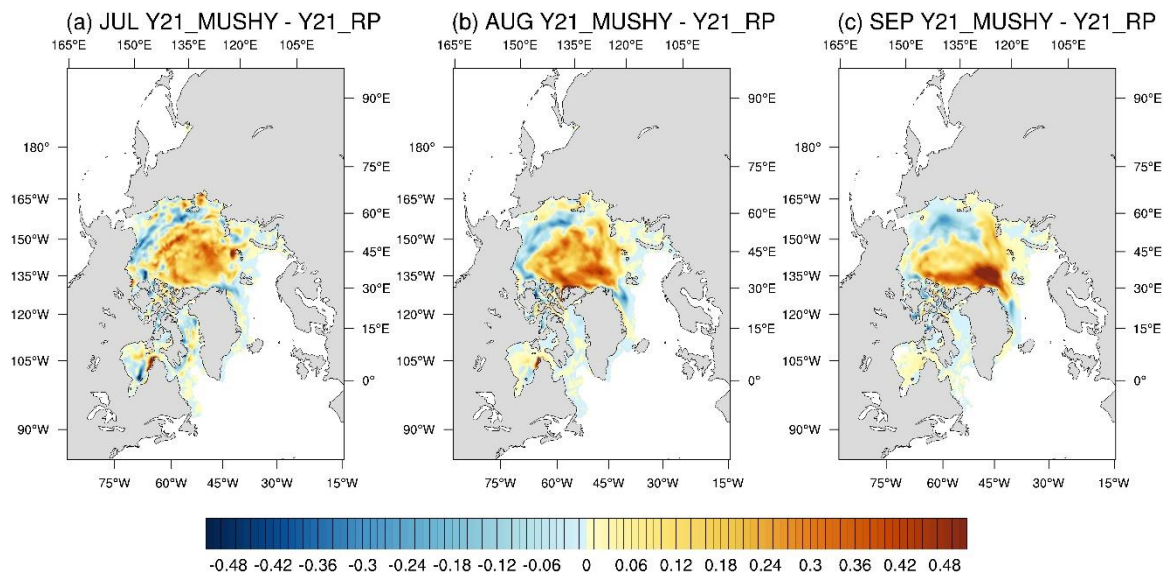




987

988 Figure 10 (a) the average temperature profile of upper 150 m under ice-covered areas for the  
989 difference between Y21\_RP and Y21\_VT. (b) same as (a), but for the salinity profile.

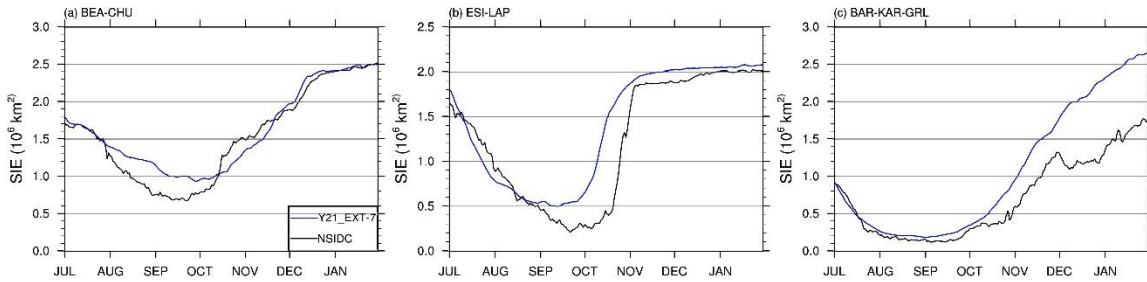
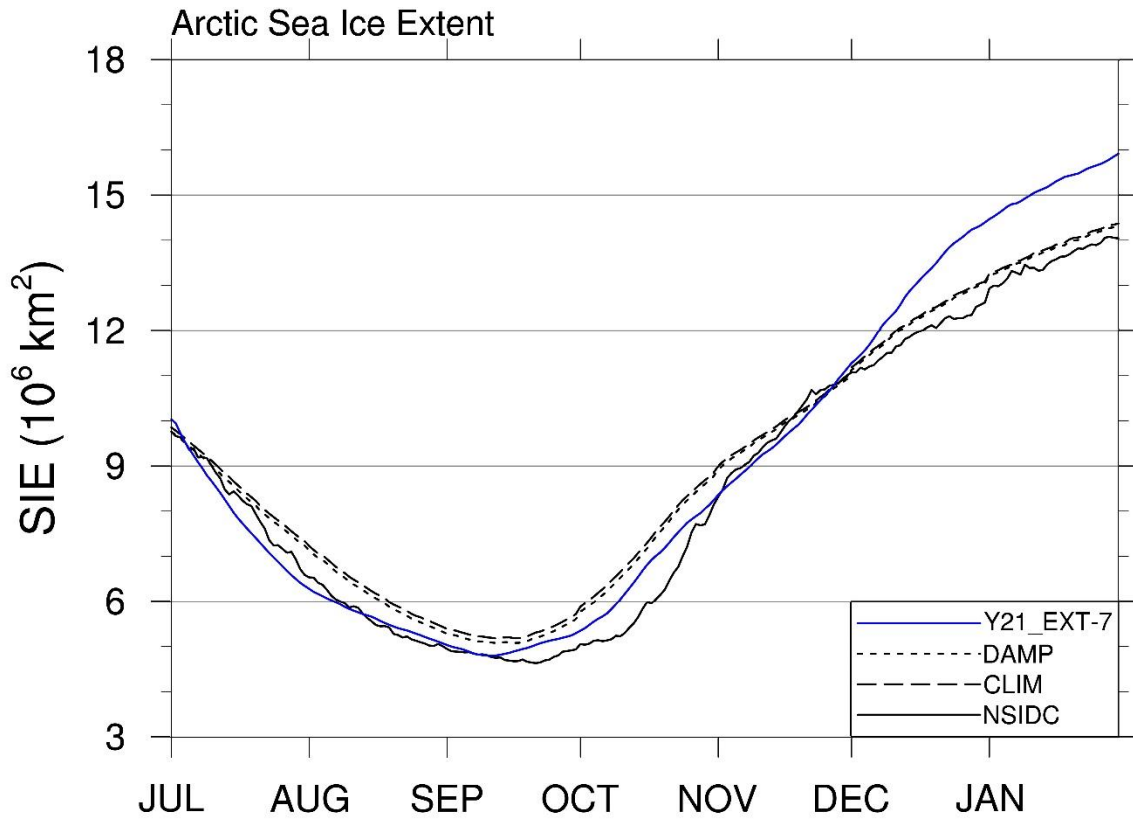
990



991

992 Figure 11 Monthly mean of sea ice thickness difference between Y21\_MUSHY (changes in

993 sea ice thermodynamics) and Y21\_RP for (a) July, (b) August, and (c) September.



994

995 Figure 12 Same as Figure 4, but for Y21\_EXT-7.

996

